The Electrical Properties of the Woodroffe Thrust: A Resistive Shear Zone

Tasman Gillfeather-Clark, BSc.

Department of Earth and Planetary Science

9th of January 2018

Statement of Originality

This work has not previously been submitted for a degree or diploma in any university. To the best of my knowledge and belief, this thesis contains no material previously published or written by another person except where due reference is made in the thesis itself.

Abstract

Shear zones are a geological feature of interest due to their unique electrochemical and structural properties. However, consensus on the causation of their conductivity anomalies at large is not unified. There are many factors to consider when understanding the electrical features of a given shear zone. Composition, including minerals and grain boundary films, as well as particle size and the presence of fluids are some key factors. Generally, shear zones are conductive in geophysical exploration and the above factors are sometimes used to explain conductivity features associated with certain shear zones. However, the cause of this conductivity is often poorly constrained.

My work uses rock samples and geophysical data gathered at a surface expression of the Woodroffe Thrust, NT, Australia. Using micro X-ray fluorescence, I evaluate compositional (mineral) and structural properties (grainsize) of my survey area. The conductivities of samples from the thrust are examined in lab conditions using electrochemical impedance spectroscopy. I then compare these conductivity values with the field geophysical data (time domain electromagnetics and magnetotellurics). By constraining the data in this way, I can consider in detail the causation and expression of the electrical response.

My conductivity results highlight a disparity between my field and lab results of over seven orders of magnitude whilst also hinting at an anisotropy of conductivity mechanisms. These results contribute to a larger narrative of conductivity, with lab/petrophysical analysis on one side and field/geophysical results on the other. My work highlights that there is no property of a shear zone that makes it inherently conductive and that understanding the electrochemical response of a shear zone requires detailed analysis.

Acknowledgements

I'd like to thank my supervisor, Kate Selway for her guidance, support and patience, throughout my thesis. Her door was always open, a privilege I fear I may have on occasion abused. Simon Clark and Anthony Lanati for their collective wisdom on Impedance Spectroscopy. I extend my appreciation to Peter Fullagar and Phil Muir for access to their expertise and their software, eMax. I would also like to thank Chunhai Wang of Sydney University for access to and training on the MTZ-35 impedance spectroscope. My thanks to Mark Lackie who lent me his TerraTEM for my field work and Manal Bebbington for trusting me with her rock saw upon my return. Timothy Murphy for my time and training on the M4 Turbine. I would also like to extend my thanks to the unnamed thousands on Matlab forums across the internet, encountering and overcoming the problems I had only just found.

To friends a family there is simply too much to say. To everyone who proof read my work and brought me food at my desk, I will remember you fondly. My parents I simply cannot thank enough, they gave me unfailing support and love. To my partner Lauren, you bring me joy, thank you for all that you are.

Contents

1 Introduction

Shear zones are known globally for their complex geology and varied geophysical expressions. Surveys over shear zones can oversimplify complex responses or in some cases are unable to resolve the detailed conductivity features. Lab measurements on the other hand are time consuming and potentially non-representative of larger geological settings. By considering lab and field results gathered in this work in parallel I hope to compare the weaknesses and strengths of both, while discussing the unique expression of the Woodroffe Thrust, NT, Australia. Comparing the results of this work with other studies will allow me to consider factors, which impact on the conductivity of rocks. Understanding the factors controlling conductivity informs interpretation which has significant economic and modelling impacts in both academic and industrial settings.

This thesis presents a range of lab and field analysis over the Woodroffe Thrust, NT. These are then used to consider the electrical properties of the shear zone and the impact of grainsize on conductivity.

1.1 Project Aims

I. Typify the electrical, mineralogical, and grainsize characteristics of the Woodroffe Thrust, NT.
II. Identify and constrain trends and features of this analysis and identify probable causes of conductivity changes across the transect if any are present.

1.2 Project Structure

Section 2 provides a background for this work, starting by covering conductivity from the practical (how it is measured) to the theoretical (controls and mechanisms), and then discusses shear zones and the geological setting of our site specifically.

Section 3 is an overview of the methodology of the techniques used in this work: micro x-ray fluorescence, electrochemical impedance spectroscopy, magnetotellurics and time domain electromagnetics.

Section 4 presents the results of the techniques covered in Section 3 and identifies key aspects and highlights them for discussion.

Section 5 builds upon the features identified in section 4 to discuss the outcomes of this work, within the context of other findings and then proposes future work, which could correct for issues encountered in this work. The aims of the thesis are reintroduced here.

Section 6 summarises the outcomes of this work and finalises key ideas discussed in section 5.

2 Background

2.1 Conductivity

The conductivity of rocks is critical to understanding the subsurface, as it informs our interpretation of the mechanisms which operate within our planet. Electrical conductivity is a measurement of a material's ability to transmit an electrical current, the mechanism for which in a geological setting varies based on the composition and structure of the rock through which the current is moving. Resistivity (ρ) is formulated below, where V is the voltage, I is the current, A is the cross-sectional area of the specimen and l is the length of the material. Resistivity has a reciprocal value conductivity; these two terms are used throughout this work consistent with conventions associated with the technique being discussed.

$$\rho = \frac{V}{I} \cdot \frac{A}{l} \tag{1}$$

2.2 Measuring conductivity

Electrical conductivity of rocks can be measured in a plethora of ways – for convenience it is easiest to divide these techniques into field and laboratory measurements. Field techniques measure both direct electrical currents (electrical methods) as well as measuring electrical fields at known locations. These fields are proportional to the electrical properties of the mediums through which the fields propagate. Maxwell's equations describe how electrical field methods can be related to subsurface conductivity (Cagniard, 1953). Laboratory techniques conversely calculate the electrical properties of the medium directly by applying an electrical load across the sample and then comparing the input to the output current, noting change in their frequency and amplitude.

The lab technique used in this work is electrochemical impedance spectroscopy (EIS), which ultimately measures the bulk conductivity of the sample over a sweep of temperatures (Katsura *et al.*, 1998; Xu *et al.*, 2000). EIS is in common usage when considering electrical conductivity on a mineralogical scale. To complete an impedance measurement, you first make a circuit where there is current flow across the mineral or aggregate sample. This is achieved by placing the sample between two electrodes and creating a potential difference. The response of the sample is proportional to many factors to be discussed, and EIS allows for the resolution of different conductivity mechanisms by plotting the real and imaginary components of the impedance (Argand Plots). However, EIS is a time-consuming process and only images the conductivity of a very small area (<10 mm^2). This inhibits meaningful understanding of how conductivity behaves on a regional setting.

Field techniques allow you to understand how conductivity varies on a regional scale. One field technique examined in this work is transient or time domain electro-magnetics (TEM). TEM generates a periodically active field by transmitting an electrical current into a loop of wire. This generates a primary field, which is then switched off and the decay of the secondary field is measured and used to infer the conductivity of the subsurface. This technique can reach depths of ~0.4 km, though this depth is proportional to the strength of the generated field and the conductivity of the ground. Magnetotellurics (MT) contrastingly is a passive, electromagnetic field-survey technique with a considerable depth of penetration (Cagniard, 1953). It has the capability to image the electrical conductivity of the entire lithosphere (depths>400 km) (Heinson and Constable, 1992; Jones and Ferguson, 2001; Simpson and Bahr, 2005). The reason it is referred to as passive is because it measures naturally occurring electrical and magnetic fields of the earth.

Both lab and field techniques have their strengths and weaknesses. EIS evaluates a known conductivity and can image different conductivity mechanisms. However, it is time consuming and may not be representative of the larger setting in which that sample was acquired. Field techniques only indirectly sample the conductivity, but are capable of inferring conductivity values at depths that it would be expensive (TEM) or impossible (MT) to sample directly for lab analysis. In order to truly understand the conductivity of the subsurface it is best to combine results from laboratory experiments with field conductivity data (Pommier 2014).

The combination of lab and field results creates a comprehensive understanding of conductivity that allows for the inference of information about subsurface systems. In the near surface, conductivity is used to highlight the presence of disseminated ore as well water in the subsurface. At depth it is used to identify and inform our understanding of larger structures as well as earth processes. In both settings these observations are possible due to the high conductivity contrast between the target and its surrounds. However, in cases where this contrast is non-apparent, constraining the factors acting upon the conductivity is imperative. Combining lab and field techniques allows us to understand the impact of variables like grainsize, and thus inform our understanding of conductivity as a whole.

2.3 Factors affecting conductivity

The relative number of charge carriers controls conductivity. Charge carriers are any particle that is free to move, carrying an electric charge, such as ions and electrons. The number and freedom of charge carriers in a substance control its conductivity.

Rocks are typically resistive with the charge carriers bound up in the crystalline lattice. However, this resistive behaviour changes due to multiple factors: temperature, presence of grain

boundary films, presence of interconnected conductive phases such as ore bodies and the presence of melt or fluids in the pore space of the rock (Selway, 2014). At higher temperatures rocks can also behave as semiconductors. The semiconductor behaviour can be associated with grains or grain-boundaries. Grain boundaries can act as either barriers to or pathways for electrical flow. Grain-boundaries can also act as capacitors, storing a small residual electrical charge (Macdonald and Johnson, 2005).

2.3.1 Conductivity at Mantle Temperatures

At significant temperatures and pressures rocks have been shown to behave as semiconductors (Coster, 1948; Murase and McBirney, 1973; Parkhomenko, 1982). These higher temperatures typically allow for the diffusion of more species from the crystal matrix. These species then are free to act as charge carriers. There are three main species: protons *(hydrogen nuclei)*, polarons *(electrons)* and ions *(higher atomic weight charged particles)* (Selway, 2014). These species are listed in increasing order of activation enthalpy.

All factors linked to diffusion are highly sensitive to temperature. Conductivity, particularly in the subcontinental lithospheric mantle, is proportional to temperature (Karato *et al.*, 1990; Yoshino *et al.*, 2006). This is of importance when considering conductivity at depth or in areas of significant geo-thermal gradient. The additional heat provides a means to liberate more species that would otherwise be unable to diffuse and act as charge carriers (Karato *et al.*, 1990). Oxygen fugacity impacts on the ability of a species to integrate with a crystal matrix (Waff and Weill, 1975). One experimental study conducted at temperatures associated with the upper lithospheric mantle (700-850 °C), and pressures associated with the upper crust (2 kbar), found that hydrogen solubility in natural olivine increases systematically with increasing oxygen fugacity (Yang, 2012).

Proton diffusion is the liberation of a hydrogen nuclei, this has the lowest activation enthalpy. As such hydrogen content has a considerable impact on conductivity in nominally anhydrous minerals (NAMs) (Wang *et al.*, 2006). The experimental work on this subject is reviewed in detail by Selway (2014). In NAMs hydrogen content is strongly related to the number of point defects in the mineral and the relative availability of hydrogen (Padrón-Navarta *et al.*, 2014). Karato (1990) attributed the high conductivity anomalies of the asthensopshere to the solid-state conductivity in olivine even if only a small amount of hydrogen was present.

Polaron diffusion involves the diffusion of an electron between ferrous and ferric iron. Polaron conduction is sensitive to iron content. In magnetotelluric (MT) data that probes the upper mantle, constraining magnesium and iron is important due their role in olivine which is a bulk mantle material (Xu *et al.*, 1998). Yoshino et al. (2012) fabricated olivine with six different amounts of iron, following the rule $[Mg_{(1-x)},Fe_x]_2SiO_4$ with x = 0.1, 0.2, 0.3, 0.5, 0.7 and 1.0. It was

found that conductivity increased with total iron content for each phase. Adding more iron essentially created a greater number of conductive pathways. These experiments were conducted at 18 GPa and 400 K to 1600 K.

Ionic diffusion involves an ion being liberated from a crystal matrix. This form of diffusion has the highest activation enthalpy. Its impact is limited to higher temperatures typically higher than 1800 K associated with the mantle (Karato and Wang, 2013). It is unlikely due to the shallow focus of this work that these effects will be encountered. However, it does show the impact of increasing iron content on conductivity.

2.3.2 Conductivity at Crustal Temperatures

Diffusion-linked conduction mechanisms are unlikely to play a significant role at near surface temperature and pressure conditions such as those considered in this work. At near surface settings, different mechanisms including the presence of pore fluids and the existence of grain boundary films are more likely to have a considerable influence over the conductivity of the rocks. These mechanisms operate by finding alternative conduction pathways as opposed to the addition of more charge carriers (Selway, 2014). The dominant mechanisms of the crust are highlighted in Figure 1, along with depths of formation of various shear zone types. The depths, temperatures and various parameters are not comprehensive but provide an illustration which will facilitate an understanding of the crucial factors to come.

Grain boundary films are a common example of an alternative conduction pathway. These can increase the conductivity by many orders of magnitude by allowing the current to flow around the grains rather than through them. These grain boundary films have varied compositions, graphite and sulphide films are among the most commonly discussed (Watson et. al., 2010; Yoshino and Noritake, 2011). However, graphite films are relatively fragile, and their conductivity is closely linked to how interconnected they are. It is very possible for these connections to be broken in retrograde metamorphic conditions, and hence the conductivity measured in the lab is unlikely to be as high as those predicted where the graphite films remain intact (Glover, 1996). Sulphides also respond with high conductivity anomalies and can exist both as massive sulphide deposits and as grain boundary films. The impact of sulphide films were first experimentally confirmed by Watson *et al.*, (2010). However, massive sulphide deposits have been in common usage as an explanation for field observations of high conductivity, associated with shear zones and thermal fields surrounding igneous intrusions (Corseri *et al.*, 2017). Worth considering is the 'quasimetallic' conduction associated with iron rich sulphide films which can form along shear planes (Jödicke *et al.*, 2004).

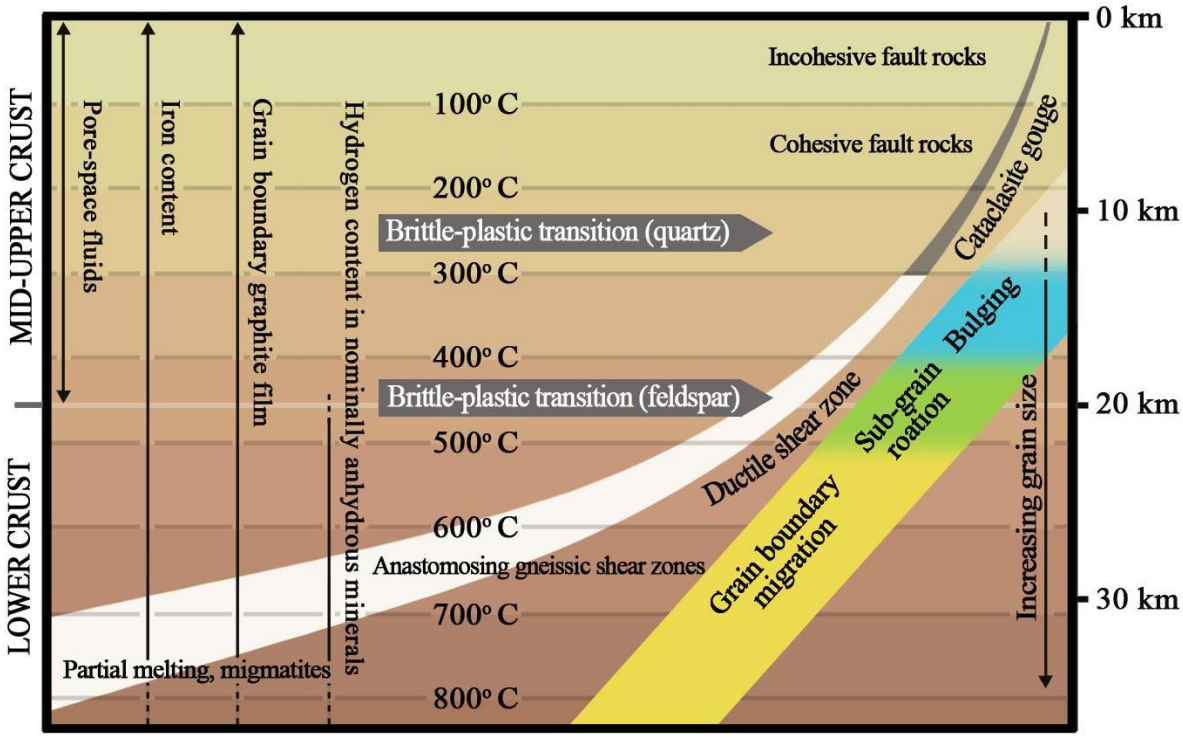

Figure 1 - Conductivity mechanisms and shear zone behaviours with depth. Figure was adapted from (Selway, 2014; Fossen and Cavalcante, 2017).

Fluids play a key role influencing the conductivity of the subsurface. Ionic conduction, as opposed to ionic diffusion, is almost exclusively associated with either melt or saline fluids. Due to this surveys cratonic setting as well as the depth to which analysis is applied, it is unlikely that my survey will encounter any melt. However, it is also possible that water may infiltrate shear zones above the brittle-ductile transition in the mid to upper crust during formation (Ritter *et al.*, 2005; Becken and Ritter, 2012).

Clay minerals are another crucial factor in near surface conductivity. To avoid ambiguity in this context I am referring to the clay mineral group that is largely composed of hydrous aluminium phyllosilicates (Borden and Giese, 2001; Nayak and Singh, 2007), as opposed to the class of granular material with the smallest grain size. Hydrous aluminium phyllosilicates have unique electrical behaviour which can cause significant electrical conductivity anomalies. Clay's electrical double layer provides an alternative pathway for electrical flow (Grahame, 1947). This flow is proportional to the cation exchange capacity which is proportional to the composition of the clay. Due to the largely anhydrous nature of the survey area I would not expect any clay group minerals. Conversely, I would expect the granular 'clay' to be present to some extent on my survey area. The effects of these detrital grains when compared to an equally fine-grained rock derived from shearing is yet to be seen.

2.4 Shear Zones and their electrical Properties

Shear zones are regions of deformation typically sub classified into brittle zones (faults) or ductile zones based on the deformation they display (Ramsay, 1980). The formation of faults and their mineral features are summarised in Figure 1. Faults from relatively low metamorphic conditions associated with the upper crust are typified by the presence of cataclasite and gouge. Ductile zones are associated with higher metamorphic conditions and the mechanisms including bulging, sub-grain rotation and grain boundary migration (Unsworth and Bedrosian, 2004; Fossen and Cavalcante, 2017). It is practical to think of shear zones relative to their depth of formation within the crust either as upper or lower crust. Figure 1 relates the type of shear at a given depth to active mechanisms of conduction, although this is a qualitative assessment.

Unsworth et. al. (2004) identified some key factors which control the geometry and resistivity of shear zones: the local geology, total offset of the fault, and hydrogeology. These factors are all focused on the ingress of fluids into the fault which characterises the conductivity. In the context of this work it is important to question if fluids are the only control acting on shear zones electrical expression. Later I will raise the possibility of the influence of grain size change as a possible influence on conductivity.

Faults have been well examined in the literature and their near surface characterisation shows a stark contrast in electrical properties. One example of a well-known brittle shear zone is the San Andreas Fault (SAF) which is a dextral strike slip fault. Various high resolution MT surveys have been conducted over the SAF showing its electrical behaviour and analysing it in detail (Unsworth *et al.*, 1997; Unsworth *et al.*, 1999; Becken and Ritter, 2012). In the most recent work cited above some theories for the cause of the high conductivity of the SAF are proposed and these include the presence of interconnected porosity networks full of fluids. These fluid pathways are typically associated with mineralisation (e.g., serpentine), and lie within wider damaged zones which are networks of cracks in the rocks which plays host to interconnected fluids. The concept of the damaged zone was introduced in Caine *et al.* (1996) and subsequently became widely used as a potential explanation for observed results (Unsworth *et al.*, 1999; Unsworth and Bedrosian, 2004; Ritter *et al.*, 2005; Becken and Ritter, 2012). These brecciated and damaged zones of the fault allow for greater ingress of water and hence higher conductivity.

However, not all faults have a clear damaged zone, nor do they necessarily have a conductive near surface expression. The Longmenshan region of China is dominated by brittle shear zones and contains a series of thrust faults on the eastern boarder of the Tibetan Plateau. MT surveys completed over this area have identified high conductivity anomalies within the Longmenshan region associated with the Longquanshan Fault and the Pengguan Fault. These anomalies are associated with near surface expression of low resistivity (10-30 Ohm m) unit

projected to the surface by these faults. The Wenchuan-Maowen Fault shows no such conductivity anomaly and is associated with a High Resistivity Body (HRB; 1000 Ohm m) (Zhao *et al.*, 2012). However, their work does not detail the cause of the HRB other than noting that highly resistive responses are expected for crystalline rocks which are present on the western boundary of the anomaly. Other work evaluating the Longmenshan shear zone confirms its resistive nature in the upper crust (Sun *et al.*, 2003) with any conductive areas being attributed to surface weathering.

Another shear zone of interest is the Dead Sea Transform (DST) centred on the strike slip Arava Fault (AF). The AF acts as a barrier between two different rock formations (Ritter *et al.*, 2003) with the electrical properties across the fault jumping approximately two orders of magnitude. The western high conductivity was attributed to sediment fill (Ritter *et al.*, 2003) as opposed to the conductive core damaged zone as discussed in the SAF. This is occurring likely in conjunction with the fault acting as a barrier to fluid migration. Despite a high-resolution survey (100 m spacing) the authors were unable to resolve a conductivity anomaly, which was likely due to the relatively narrow damaged zone associated with the AF (Ritter *et al.*, 2003). Works since then have suggested the relatively narrow damaged zone of the AF is potentially linked to the relatively low total offset of the fault (Unsworth and Bedrosian, 2004).

Thus far I have only discussed active shear zones but of course there is also an abundance of stable shear zones commonly referred to as fossil shear zones. The Woodroffe Thrust is an example of a fossil shear zone and plays host to this work. It is classified as an inactive semi-brittle shear zone and has evidence for both brittle and ductile deformation (Lin *et al.*, 2005). My analysis focuses on the anastomosing shear zone to the north of the bulk of the pseudotachylyte. No work has been done to attempt to constrain the damaged zone of the Woodroffe Thrust. Clear damaged zones are only present in brittle shears and as this is a semi-brittle, no clear damaged zone would be expected. Without an interconnected network of fractures, it would be less likely to see the ingress of meteoric fluids. Moreover, due to its tectonic setting, it is also unlikely I would see any mantle fluid sources. These points are raised here to contrast against the possible explanations for the conductivity anomaly associated with the SAF (Unsworth *et al.*, 1997). Therefore, it may be expected that this shear zone would not have a clear conductivity anomaly associated with it.

2.5 Possible effects of grainsize on conductivity

During shearing the grain size of a rock is reduced. As such grainsize varies across the area based on the extent of the shearing. This makes it an important variable to constrain for its potential effects on conductivity. Grainsize has been shown to impact on conductivity because of the diffusion of point defects along grain boundaries (Chakraborty, 2008). Despite this work very few examples exist which confirm this as a possibility (ten Grotenhuis *et al.*, 2004). The work by ten

Grotenhuis *et al.* (2004) on synthetic forsterite crystals only observed an increase in conductivity with an decrease in grainsize when particle sizes ranged between 1 and 5 μm. Other work examining grains from 5-250 μm and up to 1000 μm, observed no difference in conductivity with changing grainsize in clinopyroxene (Yang, 2011; Yang and Heidelbach, 2012). Selway, (2014) observed the only areas likely to be impacted by the findings of ten Grotenhuis *et al.*, (2004) (i.e. areas with grainsizes <10 μm), are specific settings such as shear zones. If the experimental results of ten Grotenhuis *et al.*, (2004) are applicable in this setting, then in the shear zone I would expect to see a change in conductivity associated with changing grain size. This will be revisited in the discussion.

2.6 Geological Summary of Field Location

The Musgrave Province is in the convergence point of the three main Precambrian cratonic sections of Australia and ranges in age from the middle to late Proterozoic (Aitken *et al.*, 2009). The Musgrave Province plays host to various gneissic rocks, which are mainly of felsic lithology with precursors dated ~1600 Ma (Vernon *et al.*, 1995). The geological units that make up the Musgrave Province developed during a period of high grade metamorphism, ranging from amphibolite to granulite facies in grade which occurred between 1200 and 1150 Ma.

The Musgrave Province is most notably cross cut by the east trending Woodroffe Thrust. Pseudotachylites define the surface expression of the Woodroffe Thrust (Camacho & Fanning, 1995, Lin *et al.*, 2005). This thrust separates the Fregon and Mulga Park subdomains (Figure 2, **A**), which are structurally above and below the thrust respectively (Budd, 2001). The pseudotachylyte bearing zone described in the work by Lin *et al.* (2005) is to the south of the survey area. My transect is comprised of TEM stations and samples located in the Mulga Park subdomain. The rocks are largely sub cropping over my survey area and tend to be less weathered in areas where they are more sheared.

The survey area covered in this work had its southern extent mapped (Lin *et al.*, 2005) and a small (<1 m) dolerite vein was found amongst the mylonite/ultra-mylonite zone. Whilst it is possible small intrusive igneous rocks may be expected in the area, non-were observed. Mineralogically the areas protoliths are quartzo-feldspathic gneisses. Where they remain undeformed they have large crystals of K-feldspar up to 2 cm set in a medium/fine-grained granoblastic matrix. Sub-parallel alignment of quartz, feldspar and biotite define the gneissic layering in the sheared areas (Camacho & Fanning, 1995). A more detailed analysis of the minerology and deformation history of the area can be found there, along with a detailed analysis of the Fregon subdomain and the Musgrave block at large.

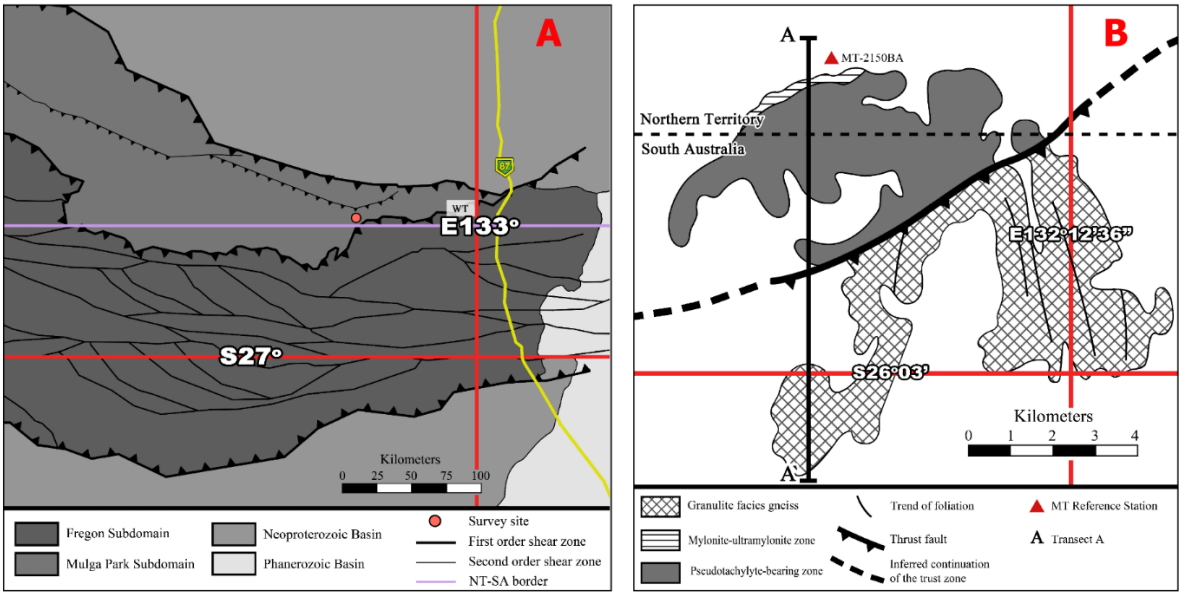

*Figure 2 – **A** Regional geological simplification of the Musgrave province adapted from Vernon et al., (1995); Lin et al., (2005) showing the field location of this work and **B** local to site geology is adapted from work by Vernon et al., (1995); Lin et al., (2005) and shows in greater detail the geology proximal to site.*

Beyond the southernmost extent of the survey, are a number of pseudotachylyte rich rocks that form the outcropping expression of the Woodroffe Thrust and south of these are a series of granulite facies gneisses from the Musgrave Orogeny (Wex *et al.*, 2015). My survey transect runs through the anastomosing shear zone to the north of the pseudotachylyte zone. A good overall geometry of the subsurface can be gauged by looking at Transect A in Figure 3 which is located on Figure 2 **B**, which shows the dip direction of the pseudotachylyte bearing zone.

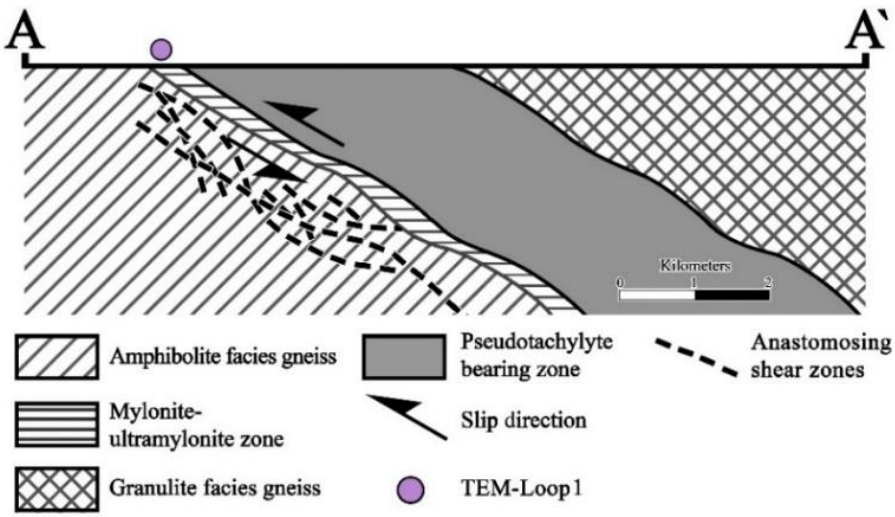

Figure 3 - This cross-section is adapted from Vernon *et al.*, 1995; Lin *et al.*, 2005*, showing the expected geometry of the subsurface. This work's southernmost TEM station is labelled with its approximate position relative to the transect.*

3 Methods

3.1 Samples

Samples analysed in this work are a combination of those originally gathered by Selway et. al. (2012) and others I gathered on a survey exclusively conducted for this work (Figure 4). The samples gathered in 2012 are a series of thin sections which act as an aid in mineral identification. The samples gathered in this work were cut and polished to create slabs ~2 cm by 3 cm and 1 cm thick. These samples were then processed for micro X-ray fluorescence and electrochemical impedance spectroscopy.

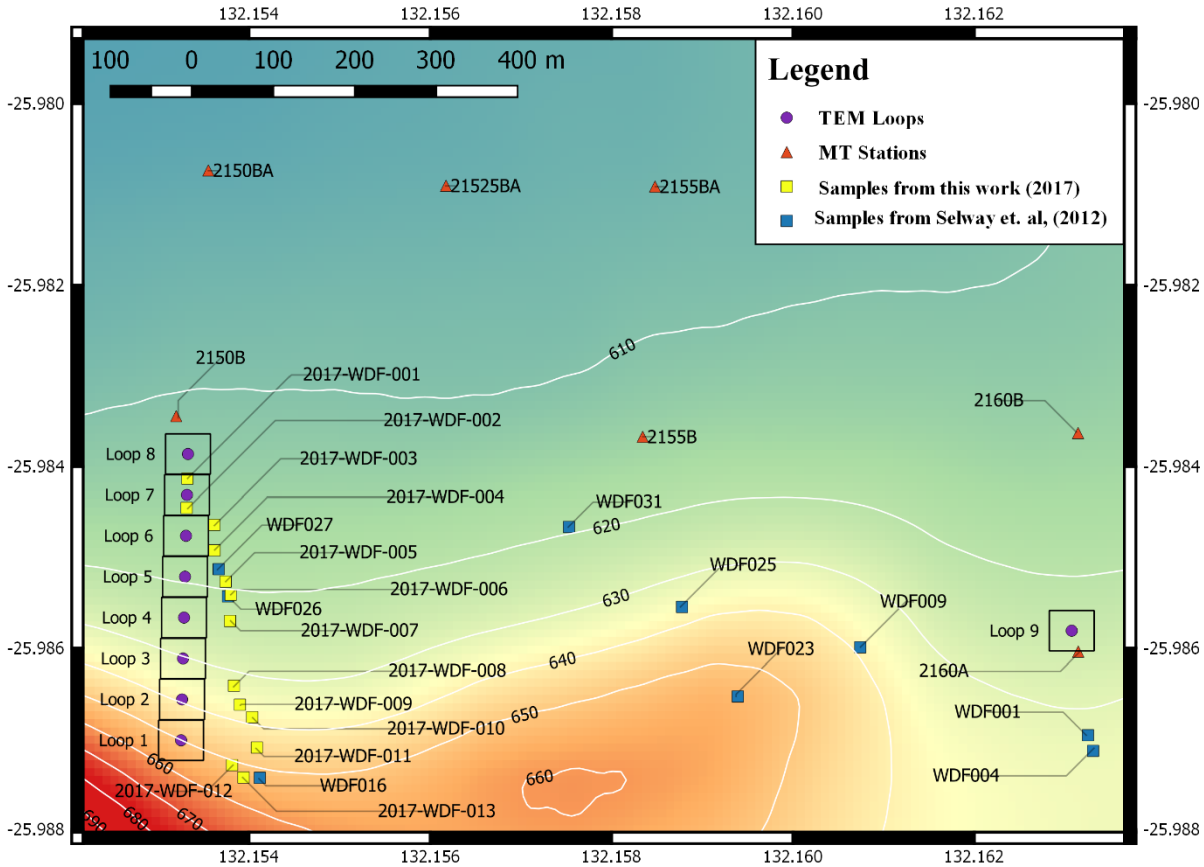

Figure 4 - Map showing sample locations used in this work. Some samples are taken from Selway et.al. (2012), while those closer aligned with the TEM loops were gathered during time on site for this work.

The goal of this sampling was to allow for lab conductivity analysis to be discussed in coming sections. My desire was to have these samples as closely aligned with the TEM stations as was possible. However, due to the lack of outcropping rock, samples were of mixed quality, typically being found exposed in creek beds.

3.2 Micro X-ray Fluorescence (µXRF)

3.2.1 Phase Analysis

X-ray fluorescence (XRF) is a non-destructive analytical technique that measures secondary x-rays emitted from a sample under examination. XRF works by measuring an emitted X-ray from a point on a sample when it is excited by a primary X-ray source. The secondary X-rays, also known as characteristic X-rays, have an excitation energy which is relative to the atomic weight of the atom they interact with. I utilised desktop micro-XRF (µXRF) which has a smaller X-Ray source beam. µXRF is seeing growing usage in earth science but particularly in mineralogical/fossil analysis (Flude *et al.*, 2016). This is because µXRF can generate phase and element maps and allow for the rapid characterisation of the mineral phases. Whilst it is possible to quantify XRF (Kanngießer, 2003) this was not the goal of this rapid characterisation. Understanding the distribution of mineral composition across the samples was key to constraining the cause of any features that could be revealed in the conductivity analysis.

The spot size was 50 microns and step size between points varied between 30-40 microns. At each point a characteristic fluorescence spectrum is acquired. The excitation energies are used to label peaks which assist in mineral identification or they can be used to produce elemental maps.

The phase data were acquired using the Bruker M4 Turbine a desktop µXRF. The goal of the phase analysis in this work was to characterise bulk mineral composition change between samples. Phase analysis was done by using Bruker's software to obtain a set of characteristic spectrums and spectrum maps. The area was then analysed in hand sample and optically, which were then correlated with the µXRF data to give a mineral phase linked to an area. My samples are 8 small polished blocks ~20 by 30 mm gathered in 2017. Where my samples were closely spatially related to the samples gathered by Selway et. al. (2012) the mineral assemblages were compared with those present in thin sections made during the 2012 analysis.

Figure 5 shows a sample slab (**A**) which corresponds to the phase map (**B**). The characteristic spectrum (**C**) is an average of what the software has identified as a single phase in (**B**). This phase analysis is done within the equipment's proprietary software. The software evaluates points with similar characteristic spectrums and plots their spatial distribution. By comparing the chemical phase, physical sample, and optical analysis I was able to identify specific minerals. This gives a more accurate representation of the composition than traditional optical methods alone.

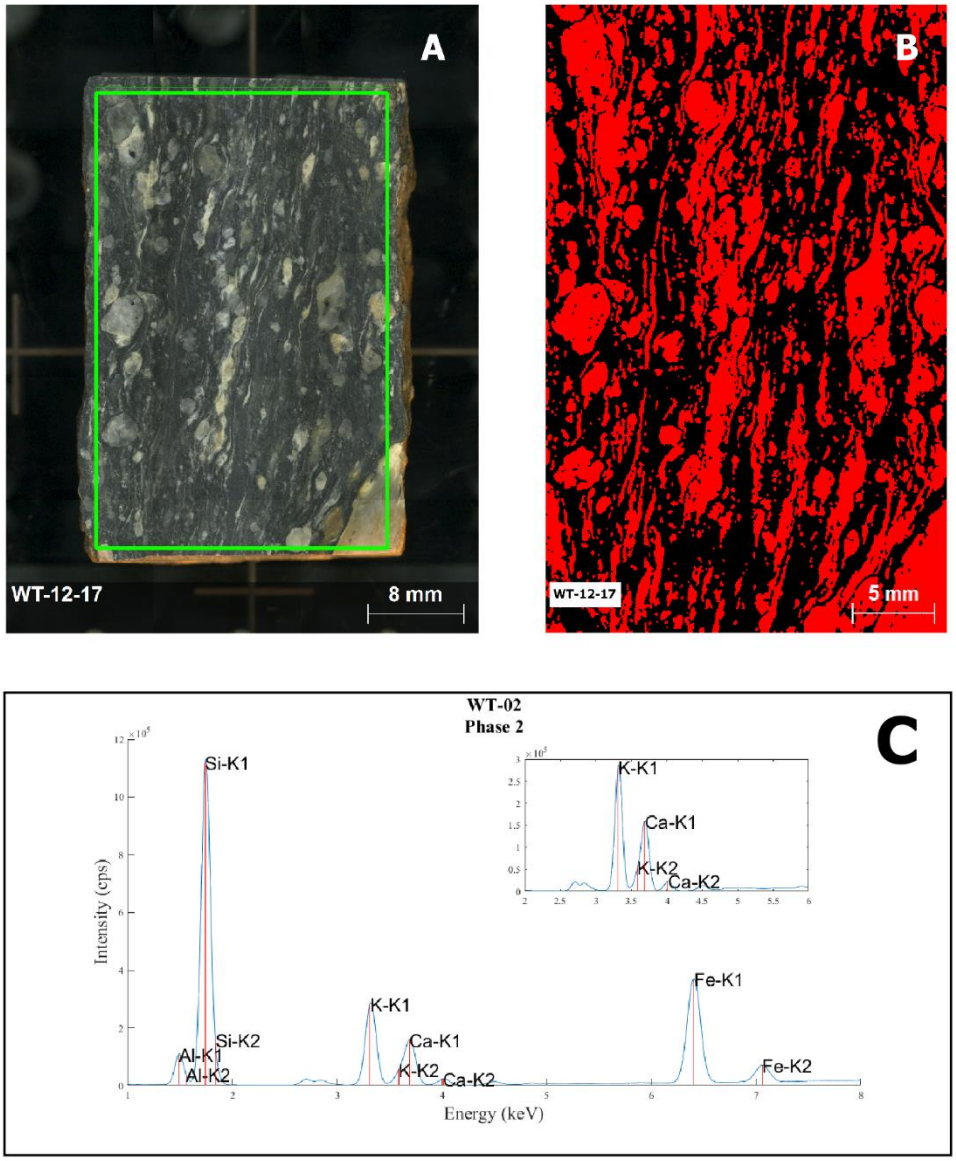

Figure 5 - The sample slab WT-12-17 ***A****, as well as a spectrum map* ***B*** *associated with a single characteristic spectrum shown in* ***C****. This area in red* ***B*** *was calculated as a percentage of the total area and compared against other phases. The red lines in the spectrum map (****C****) specify the excitation energy for a given element. The K1, K2 etc specify the peak type. The inset of plot* ***C*** *shows the peaks between 2 and 6 keV, which allows for more distinct visualisation of the peaks.*

3.2.2 Grainsize Analysis

Grain size is a structural feature which I need to constrain. Understanding its distribution is necessary if it plays a role in the measured conductivity response in crustal conditions. One of the challenges is characterising particularly small grains (<100 microns), as they are difficult to resolve from one another. This means that the groundmass can be erroneously classified as a single large grain. However, it should be noted particularly of rocks as aphanitic as those discussed in this work characterising the grainsize accurately through optical methods alone is impossible. Based on the resolution issues associated with μXRF, imposed by the spot and step size, this technique is also

non-ideal. However, it is faster and more accurate than optical analysis and has the advantage of giving additional chemical information.

To characterise the grain size above the identification threshold, I used Fiji Is Just ImageJ (Fiji) an opensource image processing software, to select several threshold layers which had intensity values which corresponded well with the various grains (Figure 6). The reason multiple thresholds are used is because distinct colour intensities tend to correspond to different minerals and hence different grains. I used elemental maps from the XRF (**A**) to create binary images (black or white) (**B** and **C**). These binary images can then be used with the inbuilt particle analysis plugin within Fiji to characterise the grainsize distribution.

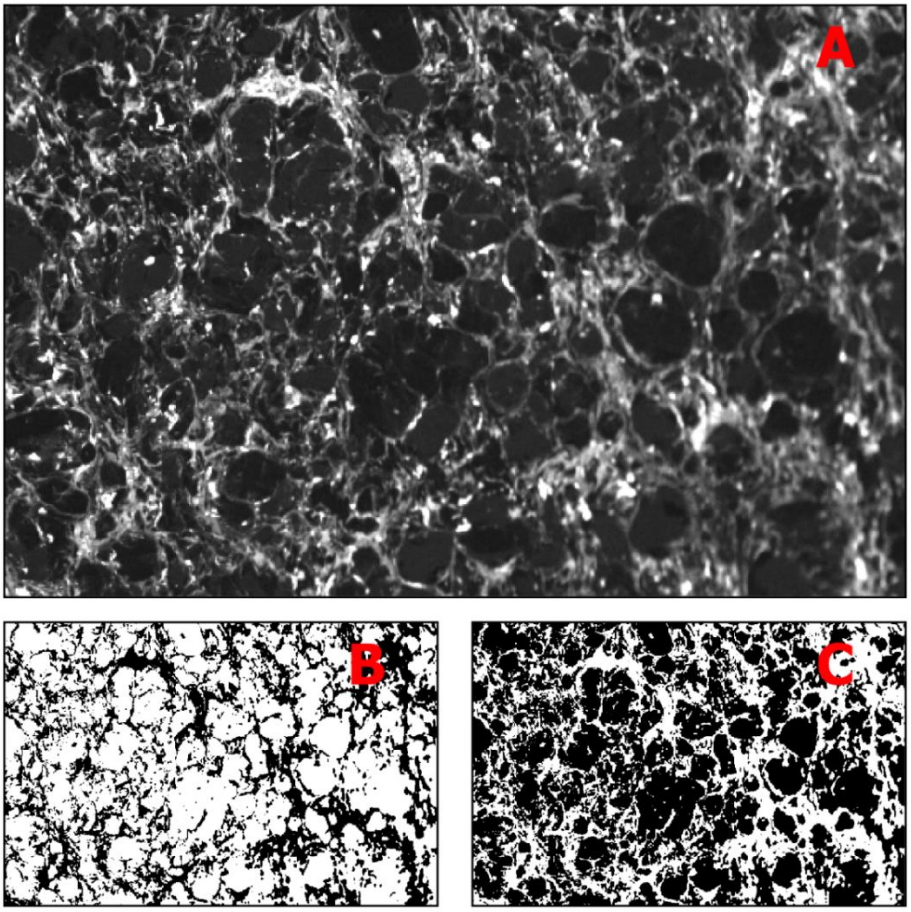

Figure 6 - An example of the thresholding outputs run over one of the mXRF images. ***A*** *is the XRF image associated with total count. This example has two dominant intensity ranges* ***B & C****, however other images contain three or more. During the thresholding process and indeed the grainsize processing at large it is important to keep check on the interpreted grainsize v grainsize in hand sample.*

It should be noted that during thresholding two key issues arise: i) grains can be artificially merged and divided ii) particularly small grains (<0.10 µm) can be lost in noise reduction. This creates a false representation of the grainsize.

Addressing the latter issue first, as discussed above the mXRF has a spot size of 50 µm. From an image processing perspective, this translates roughly to pixel size. Thus, it becomes difficult to identify a 'grain' of less than 2 pixels with any degree of certainty. It also translates to a saturation of ultrafine grains. The groundmass is commonly, extremely fine to aphanitic and is often misclassified as a single grain. This misclassification is a combination of the relatively large spot size, the relatively small grain size, and the limitations of the post processing software. To overcome this issue, the associated area was added to the groundmass portion.

The first issue is the artificial consolidation of neighbouring grains. This occurs when the image undergoing processing lacks sufficient contrast between two or more adjacent grains. When this image goes through the thresholding processes any number of grains can be merged into a single grain. To address this issue, I employed the watershed function (Soille and Vincent, 1990), which finds neighbouring outlying values and connects them.

The watershed function connects imperfections and narrow bridges between grains. The result is a collection of segmented grains which are then counted as separate grains. A typical result of the watershed function is outlined in Figure 7.

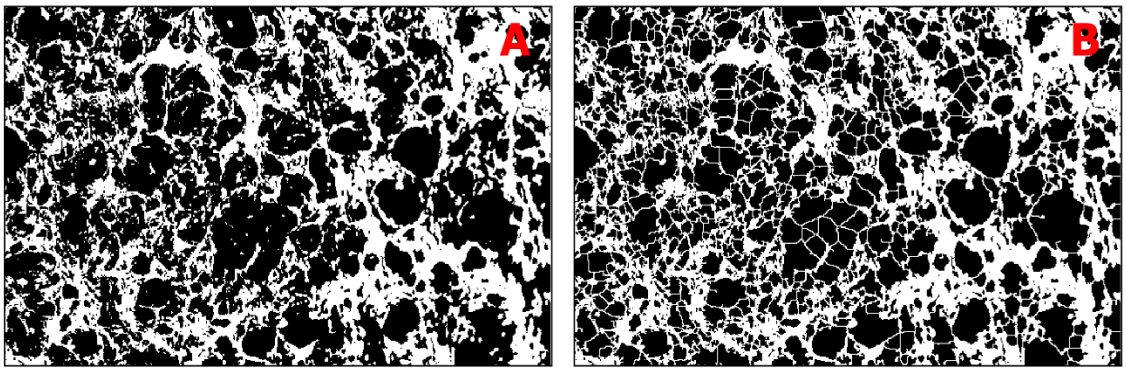

*Figure 7 – **A** depicts pre-Watershed function binary image which has been thresholded to typify the mineral grains. **B** shows the effect of the Watershed function, which has connected white points which have been separated by the black grains.*

When running the Watershed function, it is important to ensure that grains are not being fabricated. In some instances, this requires the work flow to be altered to reduce the impacts of this segmentation. One control I used was to select some of the larger grains detected by the process and compare their size as calculated by the software, with the area as approximated using measurements taken on the hand sample. These controls ensured an accurate and consistent sampling of the grain size across multiple samples.

3.3 Electrochemical Impedance Spectroscopy (EIS)

3.3.1 Theory

My ambient pressure conductivity measurements were collected in the lab using electrochemical impedance spectroscopy (EIS). EIS can be used to study any intrinsic property that influences the conductivity of a medium under study. The parameters which are derived from an IS spectrum can be understood in two main categories: i) those pertinent to the materials itself and ii) those pertinent to the material electrode interface (Lasia, 2002).

The sample or system under test has an AC sine wave of changing frequency applied to it. Measurements are then made as a function of frequency of the current (Lasia, 2002). At each frequency step the EIS analyser measures sample temperature, phase, current and the real and imaginary components of the impedance.

Impedance is formulated in Equation 2, where Z is the impedance, i is the imaginary component of the complex plane, C is the capacitor within the system, ω is the angular frequency and R is the resistor.

$$Z = \frac{R}{1+i\omega RC} \qquad 2$$

Argand plots (also known as Nyquist and Cole-Cole plots) plot the real and imaginary components of impedance on the complex plane. These plots allow you to resolve individual charge transfer mechanisms. The raw EIS data are output as the impedance-magnitude and phase at each frequency, which were used to calculate the real and imaginary impedance components. Using these values, the data were plotted in EIS Spectrum Analyser, which is a software package that plots the real and imaginary components of the impedance and calculates the R intercepts (Figure 8) and plots an Argand plot.

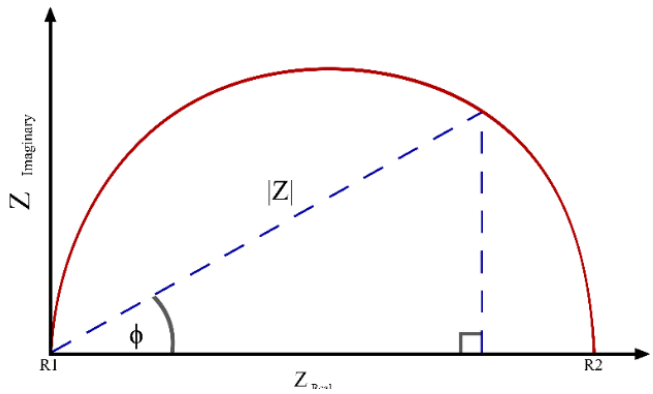

Figure 8 - Theoretical Argand Plot, showing the imaginary and real components of an ideal reading (red). The difference between the intercepts of the real axis gives the impedance value used in Equation 3.

They were fitted based on an equivalent circuit (EC) that represented the experimental data (Figure 9). An EC is representative of the physical properties of the system under investigation and is achieved by adding components to the circuit such that if the transmitted signal was passed through this EC the response signal would match that of the rock sample (Nover, 2005).

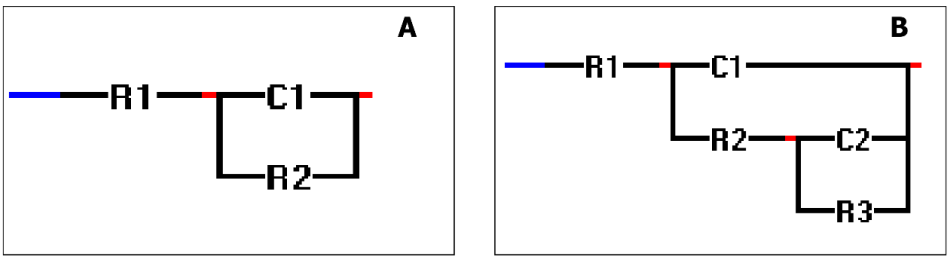

Figure 9 -The two different equivalent circuits considered in this work. ***A*** *is a three-component system where R1 is the first resistor feeding into a second resistor (R2) in parallel with a capacitive element, in this case a constant phase element (CPE).* ***B*** *is a five-component system where R1 is the first resistor feeding into a second resistor (R2) in parallel with a capacitive element C1, R2 subsequently feed into the second capacitive element C2 and third resistor R3.*

These values are then used to calculate the electrical conductivity. Electrical conductivity is determined using the simple relation:

$$\sigma = \frac{A}{R\delta l} \qquad 3$$

Where R is the resistivity value determined directly for the Argand plot which equals the difference between R1 and R2 (Figure 9**A**), δl is the thickness of the sample and A is determined by the active area of the sample in this case the diameter of the electrode.

3.3.2 Description of Equipment

EIS data were gathered using the MTZ-35 by BioLogic Science Instruments, used in conjunction with its accessory the High Temperature Furnace (HTF-1100). It is capable of measuring over an impedance range between 10 μHz to 35 MHz and using the furnace can measure temperatures up to 1100°C. Initial testing involved changing the operational voltage until sufficient points were plotted at low temperatures. This testing indicated an ideal operational voltage of 0.5 V AC. Readings were then taken every 100°C up to 800°C and back down to 100°C, over a frequency range of 0.1 Hz to 10 MHz.

Figure 10 is a schematic of the sample holder, with the sample cell inset. The sample (**d**) is placed in the sample holder (**1**) between two electrodes (**b**). The active diameter of these two platinum disc electrodes is 6 mm. The sample holder is air tight allowing the atmosphere to be controlled using a quartz tube (**2**) and I used argon gas pumped through (**4**) to limit water uptake. The sample is raised to a predefined temperature and then the MTZ-35 alters the frequency of the

current being passed through the sample at a fixed amplitude. A thermocouple (**c**) is used to measure the temperature of the system, whilst the outgoing signal from which I calculated the impedance takes the form of four components (**8**).

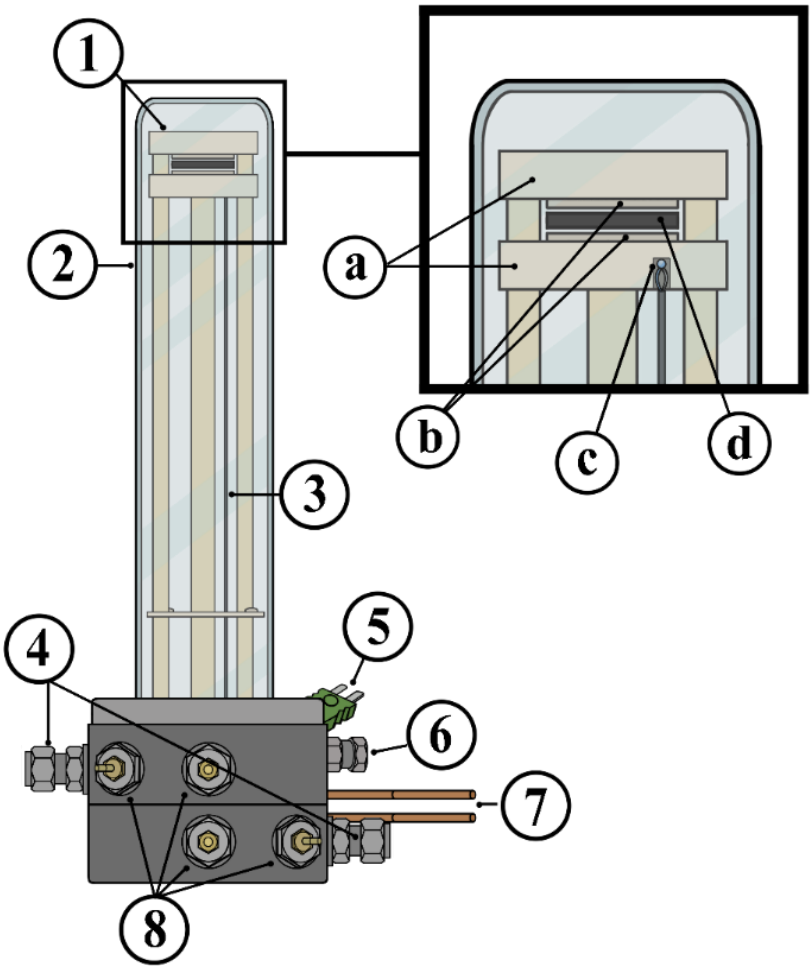

Figure 10 - Schematic of the MTZ-35 Impedance Analyser sample holder adapted from a visualisation in the MTZ-35 user manual.

Item	Description	Item	Description
1	Head – Sample is Placed in here	**5**	Sample Temperature Connector
2	Quartz Tube	**6**	Check Valve
3	Sample Temperature Sensor Wire	**7**	Cooling Pipes
4	Inert Gas Inlet/Outlet	**8**	Electrical Cell Connections

Item	Description	Item	Description
a	Ceramic Housing	**c**	Thermocouple Type K
b	Electrodes	**d**	Sample/Material Under Test

3.3.2.1 Note on Sample

Figure 11 is a 3D rendering of WT-03-17, which received the most analysis of all the samples in my work. My samples were first cored using a diamond drill core with an internal diameter of 17 mm. They were then cut with a precision saw to thicknesses less than 1.5 mm. However, this proved a challenge, particularly in the coarser grained samples which crumbled as they were prepared. Thinner samples were preferential to ensure that the results were reflective of the true impedance by ensuring the sample reached a uniform temperature throughout. WT-03-17 was the only sample to have its conductivity measured in two orientations: Blue is the conductivity measured with the foliation of the rock and Red is perpendicular to the foliation.

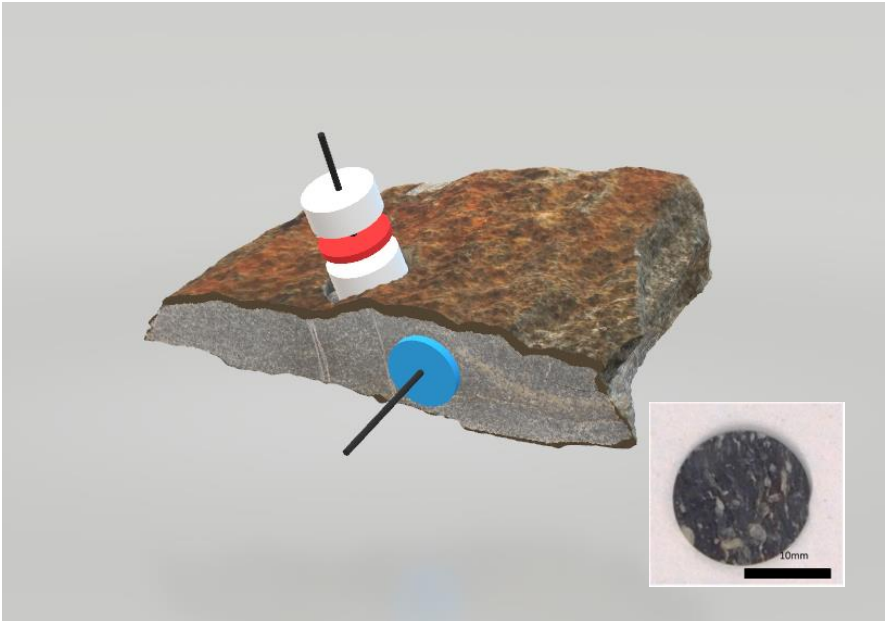

Figure 11 - Sample WT-03-17 where the red and blue disks represent the location where the samples were taken. The insert shows an example of one of the disks with scale.

3.4 Magnetotellurics (MT)

3.4.1 Theory

Magnetotellurics (MT) detects variation in the distribution of the electrical properties of the Earth's subsurface. MT uses naturally occurring electrical and magnetic fields as signal sources. At longer periods (>1 s) the source of the signal is the interaction of the solar wind with the Earth's magnetic field. At shorter periods (<1 s) world-wide thunderstorm activity generates the signal (Simpson and Bahr, 2005). It is also possible to have local interference caused by things such as power lines (Szarka, 1987; Simpson and Bahr, 2005). When a primary electromagnetic field reaches the Earth's surface a portion of this signal penetrates the Earth. This field induces electric or telluric currents

which then produce a secondary magnetic field. MT measures both the magnetic field $B_{(t)}$ and the induced electrical field $E_{(t)}$ simultaneously.

The electrical properties (e.g. conductivity) of the subsurface can be determined by the relationship between the measured electric and magnetic fields. Both the electric and magnetic components are typically measured in two horizontal components ($E_{(x)}$, $E_{(y)}$ & $B_{(x)}$, $B_{(y)}$) and potentially a vertical magnetic field component ($B_{(z)}$), where x and y are orthogonal horizontal directions. In electrically two-dimensional settings, the MT fields decompose into the transverse electric (TE) and transverse magnetic (TM) modes. The TE mode has the electrical field polarized parallel to the strike direction whereas the TM mode has the magnetic field polarized parallel to the strike direction. Using the relationship between the electrical and magnetic fields the impedance (Z) can be calculated using Equation 4 (Simpson and Bahr, 2005).

$$\begin{bmatrix} E_x \\ E_y \end{bmatrix} = \begin{bmatrix} Z_{xx} & Z_{xy} \\ Z_{yx} & Z_{yy} \end{bmatrix} \begin{bmatrix} B_x \\ B_y \end{bmatrix} \qquad 4$$

The depth of penetration of these techniques is proportional to the oscillation frequency of the electromagnetic field. The skin depth (delta, Equation 5) is derived from the components of the electric and magnetic fields, where ρ is the apparent resistivity (Ohm-m) and T is the period (Simpson and Bahr, 2005).

$$\delta = \frac{\sqrt{2}}{\mu_0}\sigma\omega \approx 500\sqrt{\rho T} \qquad 5$$

In a uniform half-space, the true resistivity is given by Equation 6, where T is the period, Z is the impedance and μ is the magnetic permeability.

$$\rho = \frac{T}{2\pi\mu} \cdot |Z|^2 \qquad 6$$

When the resistivity is non-uniform, the above equation no longer gives true resistivity but apparent resistivity, which is frequency (period) dependant. This is the case in real data and in layered 1-D, 2-D or 3-D settings. For each additional dimension the impedance can be reduced to the expressions mentioned (1-D, 2-D or 3-D) based on the electrical feature being imaged.

1-D features are the same in both the x and y dimensions with no lateral variation in the conductivity values. Hence in a 1-D setting considering Equation 2 the diagonal elements of the

impedance tensor Zxx = Zyy=0 as they are parallel to the electrical and magnetic field components. Meanwhile the Zxy and Zyx components would be equal but have opposite signs. In a 2-dimensional setting the impedance will vary vertically and laterally in one direction. Therefore, in a 2-D setting Zxy ≠ -Zyx but the data could be oriented so that the x or y direction is aligned along the electromagnetic strike, in which case Zxx and Zyy will return to zero. This is not always possible due to 3-D induction or distortion (Simpson and Bahr, 2005). Ultimately in a 3-dimensional setting the impedance varies in all directions.

One of the key assumptions of MT is that accumulations of free charges are not sustained within a layered earth. In a multidimensional earth, charges can accumulate along discontinuities. This generates a non-inductive (galvanic) phenomenon known as static shift. Static shift manifests due to under sampling in the space domain. Static shift can be caused by any multi-dimensional conductivity contrasts and its time independent nature means there is no impedance phase associated with it (Simpson and Bahr, 2005). This means while the apparent resistivity curves between stations will clearly be offset, the phase plots will show a good correlation. Static shift can be corrected for by using active near-surface measurements such as time domain electro-magnetics (Sternberg *et al.*, 1988).

3.4.2 Acquisition

The dataset used in this work was gathered in a previous body of work (Selway *et al.* , 2012). The outcome of that work was a 2-D explanation of some interesting negative phases in the TE MT data. It was collected over the Woodroffe Thrust and consisted of a grid of 28 stations with spacings between 250-500 m. Four component data were collected with two horizonal orthogonal electrical and magnetic fields. The magnetic fields were measured with induction coil magnetometers and the two electrical fields were collected using porous copper/copper sulphate pots as electrodes. Figure 12 shows the entire MT grid collected by Selway *et al.* (2012).

The analysis in this work focuses primarily on the 2150 line which consists of four stations (2150B, 2150BA, 2150C, 2150D). The Selway *et al.*, (2012) dataset had a period range between 0.008 -26.214 s. Due to my focus on the near surface I limited the period range to between 0.008-1.02 s as longer periods correspond to depths which I am not interested in. Selway *et al.* (2012) showed that at periods shorter than ~1 s the structures in the area are 2D and the strike direction is approximately 90°. Since data were collected with electric and magnetic axes oriented north-south and east-west, the MT data does not require rotation.

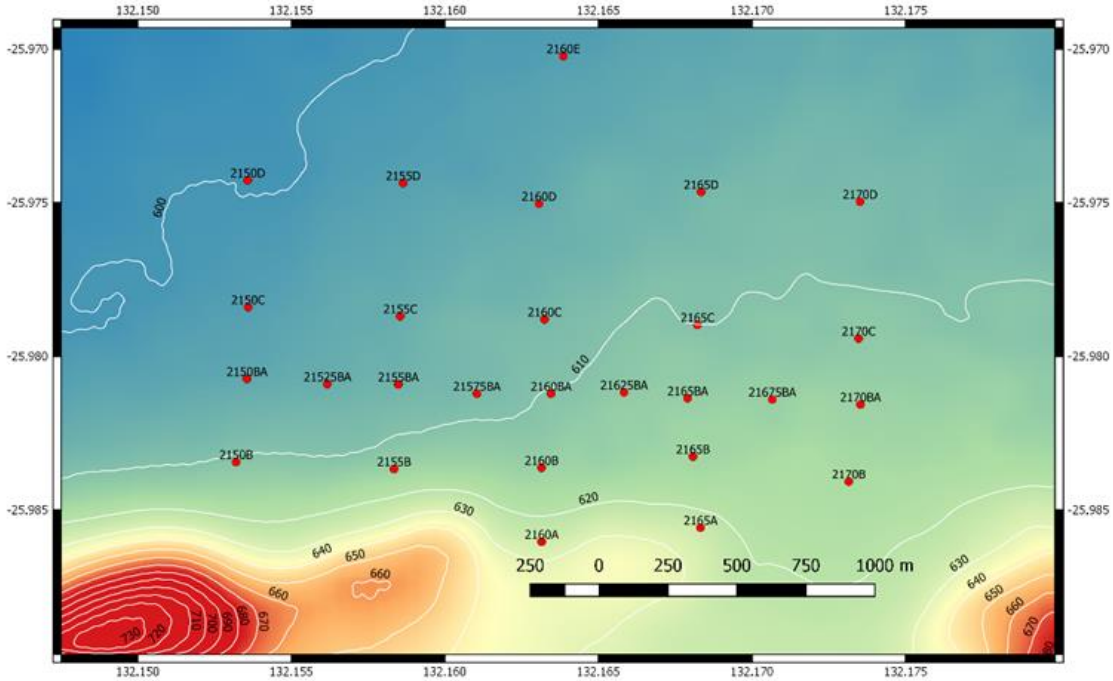

Figure 12 - Map showing the distribution of MT sites over a DEM of the survey area gathered by Selway et.al. (2012).

3.5 Transient or Time Domain EM (TEM/TDEM)

3.5.1 Theory

Transient or time domain electro-magnetics (TEM) is a geophysical survey technique which uses a periodically active source to induce a field in the ground. The field is generated by transmitting a current into a loop of wire (Nabighian and Corbett, 1991). The primary field is then switched off, the surface currents decay due to ohmic loss, and the decay of the secondary field is measured. I used TEM because it allows for the acquisition of quick high resolution electrical data, it also allows me to perform static shift corrections to the MT data which has been shown to drastically improve the accuracy of MT data (Sternberg *et al.*, 1988).

The response is generally a mathematically complex function of conductivity and time. However, during the late stage, the mathematics simplifies considerably as in Equation 7, where e(t)=output voltage created by a single-turn receiver coil of area 1 m^2, k_1 = constant, M=product of the transmitted (Tx) current · area of loop (m^2) and σ = terrain conductivity (S/m) t is time(s).

$$e(t) = \frac{k_1 M \sigma^{3/2}}{t^{5/2}} \qquad 7$$

3.5.2 Acquisition

TEM data were collected over two days in central Australia in May 2017 using a Monex terraTEM unit. The terraTEM is a transient electromagnetic survey system with inbuilt transmitter and receiver. The transmitter outputs a square wave of alternating current and a ramp up time approaching zero seconds. The locations can be found in Figure 4. Each station consisted of a

rectangular coincident loop with 50 m sides, giving an effective area of 2500 m^2. Data were recorded using the channel times specified in Table 1.

Channel Times Used in Terra TEM							
DELAY	WIDTH	DELAY	WIDTH	DELAY	WIDTH	DELAY	WIDTH
0.0015	0.002	0.0525	0.008	0.4085	0.064	2.8085	0.512
0.0035	0.002	0.0645	0.016	0.4725	0.064	3.3205	0.512
0.0055	0.002	0.0805	0.016	0.5685	0.128	3.8325	0.512
0.0075	0.002	0.0965	0.016	0.6965	0.128	4.6005	1.024
0.0105	0.004	0.1125	0.016	0.8245	0.128	5.6245	1.024
0.0145	0.004	0.1365	0.032	0.9525	0.128	6.6485	1.024
0.0185	0.004	0.1685	0.032	1.1445	0.256	7.6725	1.024
0.0225	0.004	0.2005	0.032	1.4005	0.256	9.2085	2.048
0.0285	0.008	0.2325	0.032	1.6565	0.256	11.2565	2.048
0.0365	0.008	0.2805	0.064	1.9125	0.256	13.3045	2.048
0.0445	0.008	0.3445	0.064	2.2965	0.512	15.3525	2.048

Table 1 - Delay of the channels after the Tx current is turned off and the width or time the measurements averages the signal over.

Nine stations were recorded with an average transmission current of 4.5 Amps. Typically, three soundings were made at each loop (Table 2). This, along with large numbers of stacks was done to increase the signal to noise ratio. After a noted increase in the noise in the early channel times at Loop 2, it was decided to increase the number of stacks to correct for this error. Observation of the data on site, showed this mitigated the issue.

	LOOP 1	LOOP 2	LOOP 3	LOOP 4	LOOP 5	LOOP 6	LOOP 7	LOOP 8	LOOP 9
AMPS	3.97	4.54	4.58	4.64	4.7	4.58	4.49	4.44	4.16
STACKS	512	1024	1024	1024	1024	1024	1024	1024	1024
SOUNDINGS	3	3	3	3	3	6	5	3	3
DATE	24/05	24/05	24/05	24/05	24/05	RPT	25/05	25/05	25/05

Table 2 - Tx current, number of stacks, number of repeats and the date of each reading taken during the TEM survey.

Loops 1-8 form a north-south transect where each successive loop shares a side. Loops 8 and 9 correspond to MT stations gathered (Selway *et al.*, 2012) so that these stations can be used to constrain the near surface conductivity of the MT data. Loops are named in order of acquisition and Loop 6 was repeated on both days, ensuring consistency between the two days. The transect cross cuts multiple small creeks/runoffs, whose size is not revealed by the DEM in Figure 4. Generally, noise was constrained to spiking values in early channel times. Overall the survey area was dry and even creek beds showed very little signs of moisture. As was discussed in Selway *et al.* (2012) southern stations (Loops 1-3) had sub-cropping rock indicating that basement was not very deep below the surface and sedimentary cover thickens heading north.

4 Results

4.1 µXRF

4.1.1 Mineral Characterisation

Whilst most of the mineral analysis was done via the µXRF it was important to confirm the presence of these minerals in hand sample (Figure 13) and using petrographic analysis. This was done by examining two samples from (Selway *et al.*, 2012), whilst these samples were gathered over different surveys they were found at near identical locations. As such Figure 14 compares WDF-26 and WDF-27 to WT-06-17 and WT-04-27.

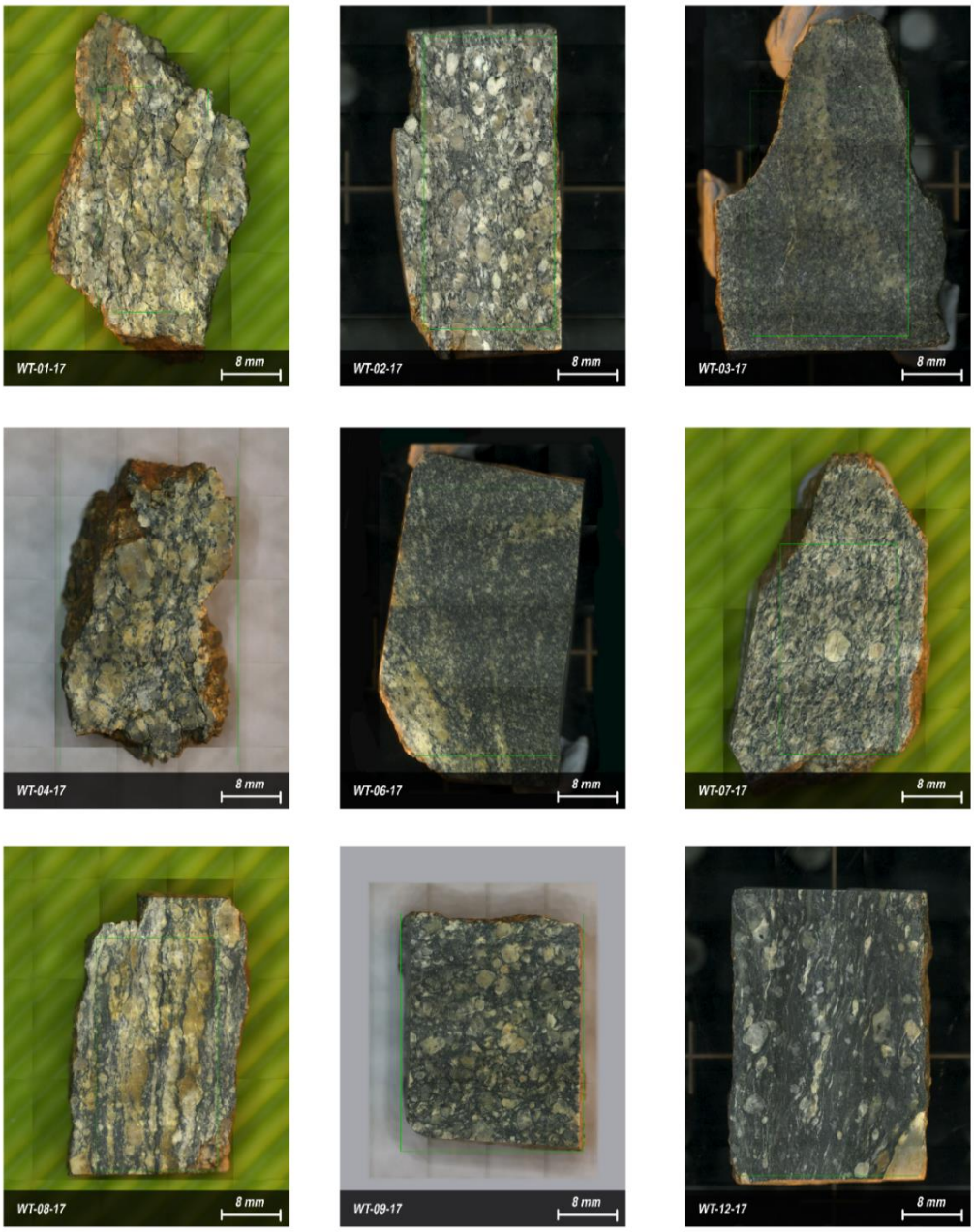

Figure 13 - The 9 samples analysed with µXRF. Each of these samples has an associated mineral phase and grain size characterisation.

This optical analysis was to identify minerals which were noted from literature on the area and confirm their presence. Figure 14 samples are a combination of **A** K-feldspar, **B** quartz, and **D** Ca-feldspar. Whilst in Figure 14 muscovite **C** is identified, it is in smaller amounts (<1% across the samples). The opaque mineral imaged in Figure 14 **E** and **F** is pseudotachylyte.

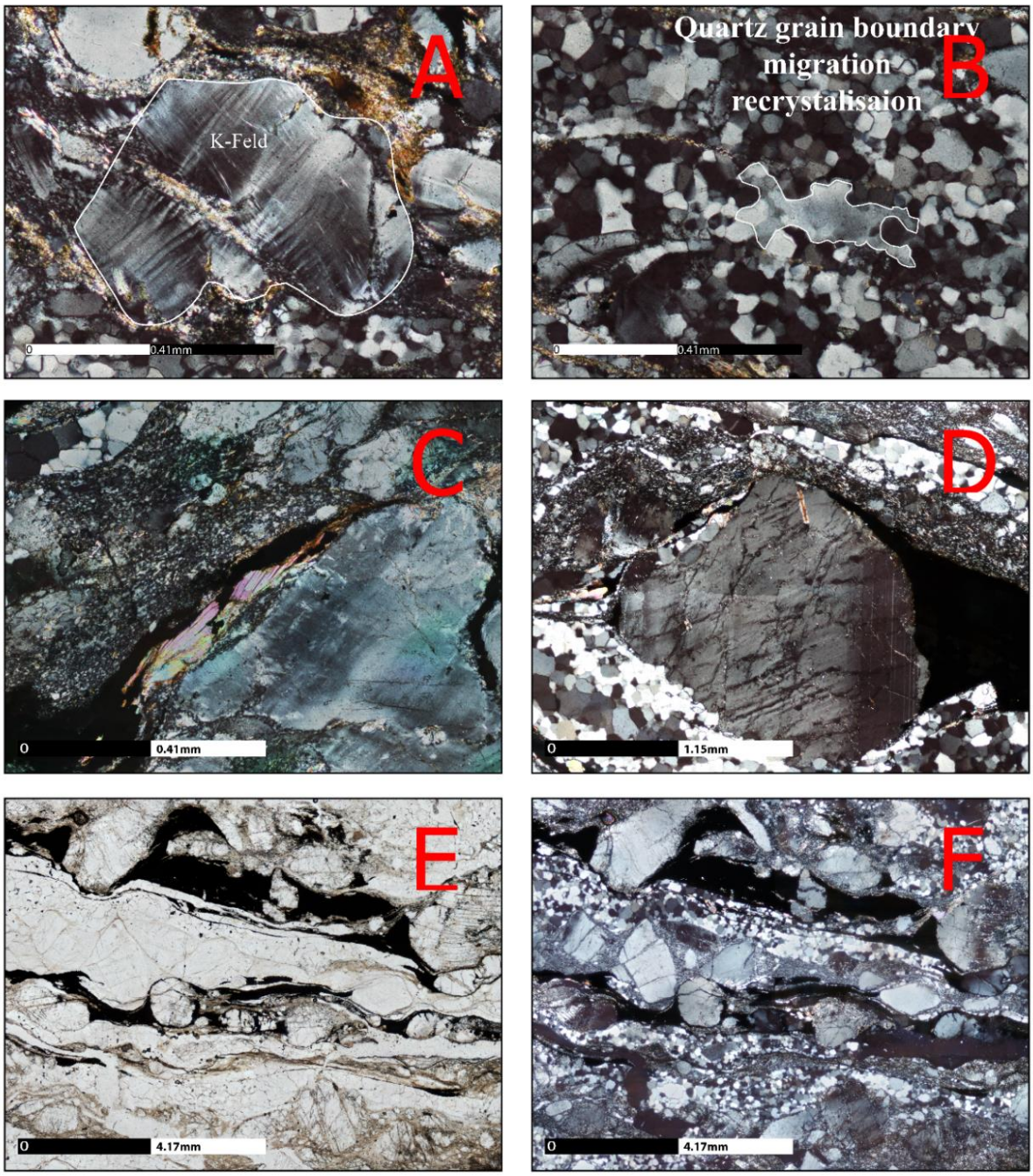

Figure 14 - A: deformed K-feldspar, B: recrystallized quartz, C: small amounts of muscovite, D: Ca-Feldspar. E-F show a fine grained opaque likely pseudotachylyte in plane polarised light and cross polarised light

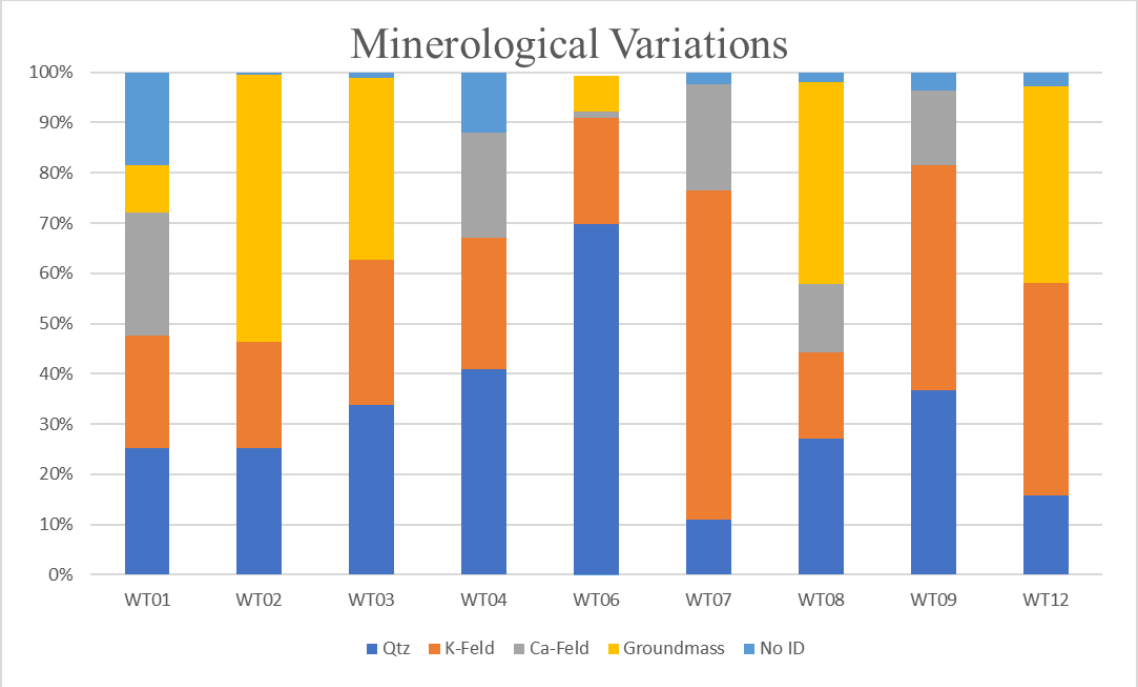

Figure 15 - The percent composition as calculated from the elemental phase maps and characteristic spectrum plots. Groundmass in this context refers to grains which were resolved as having spectrums which were of intermediate composition between the identified phases. No-ID are a combination of cultural features endemic to each sample (e.g. cracks in the sample's surface).

The characteristic spectrums for each of the key phases identified above are plotted in Supp.Figure 1-Supp.Figure 4. Each considers only one spectrum per phase for the sake of expediency. It is also important to recall that XRF struggles to detect light elements, so clear peaks for elements lighter than sodium are not expected. Each spectrum is typified by a notable peak (Si, K, or Ca) and all spectrums have a high iron peak. The characteristic spectrum that was identified as groundmass (Supp.Figure 4) is typified by the distinct elemental peaks, which do not directly correspond with a specific mineral phase. It is likely that this phase corresponds to a merged response of multiple aphanitic grains which are being averaged by the relatively large spot size.

Figure 15 summarises the mineral composition of the samples. Some samples have a phase characterised as having no ID. These are features endemic to each sample which are not associated with minerals. Samples with less than 5% of their phases noted as No ID are unlikely to have any distinct effect on the conductivity in either a field or lab setting. However, sample WT-01 and Sample WT-04 need to be addressed, consider the physical samples in Figure 13. Sample WT-01 is highly fractured. The phase calculation software identified the fractures as multiple unique phases (Figure 16 **A**) cumulatively they accounted for ~10% of the sample. WT-04 is another heavily weathered sample, which has quite an irregular shape. The XRF software incorrectly identified the sides of the sample as an additional phase, which is obviously not associated with a

mineral phase (Figure 16 **B**). Overall the composition across the transect shows no mineral variance in the phases present, though the proportions change with no clear pattern.

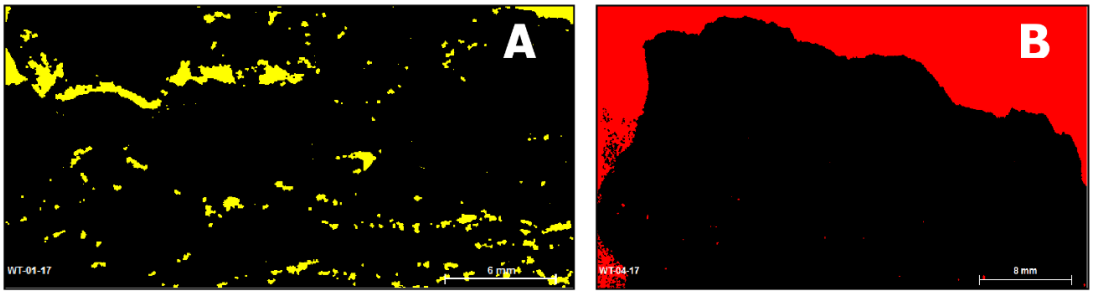

Figure 16 - The above shows some examples of areas identified as No-ID. ***A*** *is from sample WT-01-17 and the area in yellow corresponds to fractures in the rock.* ***B*** *is from WT-06-17 and corresponds with the outline of the sample and does not represent a true phase.*

4.1.1.1 Note on Iron Films

It is also important to briefly discuss the distribution of iron using the elemental maps as it was as a notable peak in all the phases. The iron is concentrated in the matrix. This helps in explaining how it manages to end up in every phase, as any fine-grained phase would be integrated into the phase due to spatial aliasing caused by the relative spot size. However, this does not explain a source for the iron content. No mineralogy in the area is indicative of iron and indeed even optical analysis reveals no minerals which could potentially explain the iron content.

A possible explanation could be the ingress of iron from surface fluids filtering down into the rock via pore space. Whilst this would explain the distribution, some of these samples are exceptionally resistant to weathering Figure 17 shows sample WT-12-17 which was the most resistant to weathering at the southern end of the transect and it seems to show the highest relative abundance of an iron rich matrix. Therefore, it is unlikely that the source of this iron is from surface ingress. There is also little evidence for metasomatic alteration in the area, so it is also unlikely that this would be a potential source for the iron.

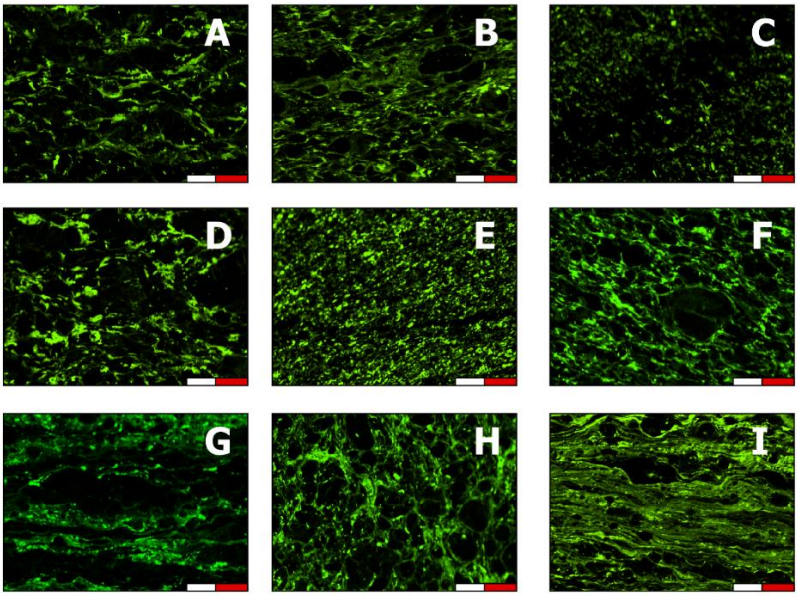

Figure 17 - Iron elemental maps across all samples. This figure contains no count information. It is only useful for highlighting the distribution of iron from a minerals/groundmass perspective. The scale in the figure has a total length of 3 mm.

4.1.2 Grain Size analysis

The results of the grain size analysis are summarised in Figure 18. Overall the transect I surveyed in the Mulga Park subdomain is extremely fine grained with all samples having over 60% of their grains less than 1 mm^2. This grain size characterisation as mentioned in the methods, does not consider grains <0.1 mm^2, due to the initial data's resolution.

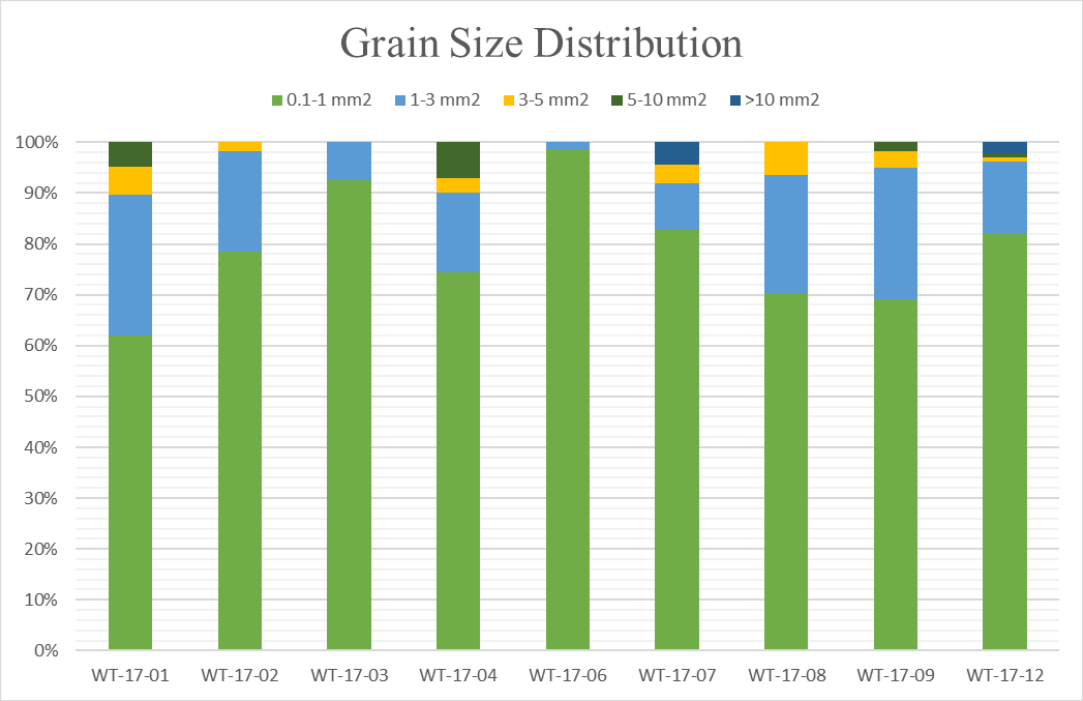

Figure 18 - Stacked bar graph showing percentage area composition by grain size.

Whilst the primary goal of the grain size analysis was simply to determine grainsize variation, the process also gives great illustrations, which allow you to consider the fabric of the rock you are analysing. This is illustrated in Figure 19.

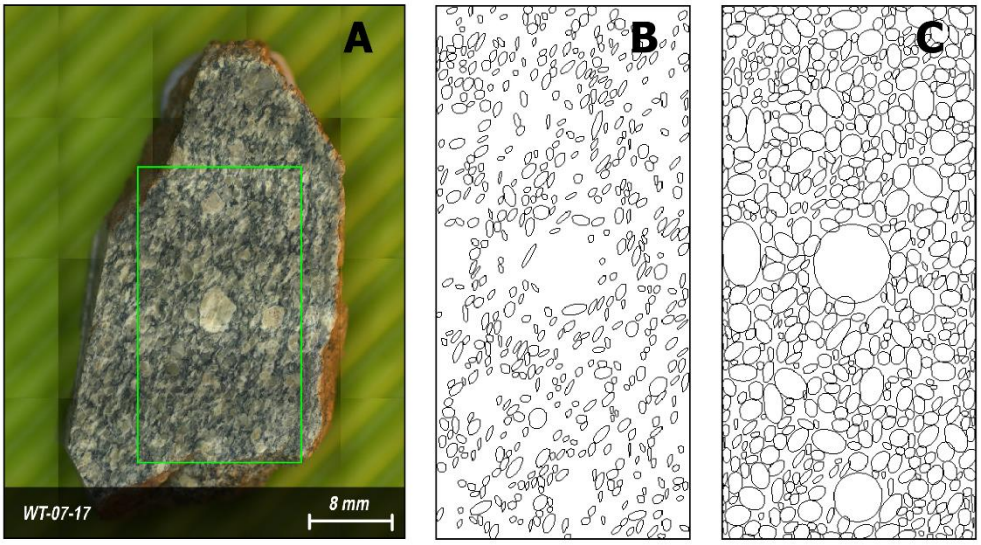

*Figure 19 – Example showing a sample **A** next to illustrations **B & C** generated through the work flow which visualise the fabric of the rock.*

4.2 Electrochemical Impedance Spectroscopy (EIS)

The following Argand plots are used to calculate the R value from Equation 3 to solve for the conductivity of a given reading. They also provide qualitative information regarding the number of conductivity mechanisms acting on a single reading, as the curves correspond to different mechanisms of conduction. In complicated settings, decisions on to how to model the data and subsequently which equivalent circuits to use, can only been made after examining the data (Macdonald and Johnson, 2005).

Examining this data reveals it behaves as the three-component system described above, comprised of two resistors and a constant phase element. It is possible to see the beginning of a different conductivity mechanism in some readings taken at temperatures greater than 600°C. Its occurrence is inconsistent across samples, where it does occur there is mostly insufficient data to model the intercepts with certainty. As such these tails seen in Figure 20 **D** and **F** were not used in the calculations but instead noted as qualitative evidence for additional conductivity mechanisms. Examples of the curve fitting process at different temperatures can be found in Figure 20 with the EIS results.

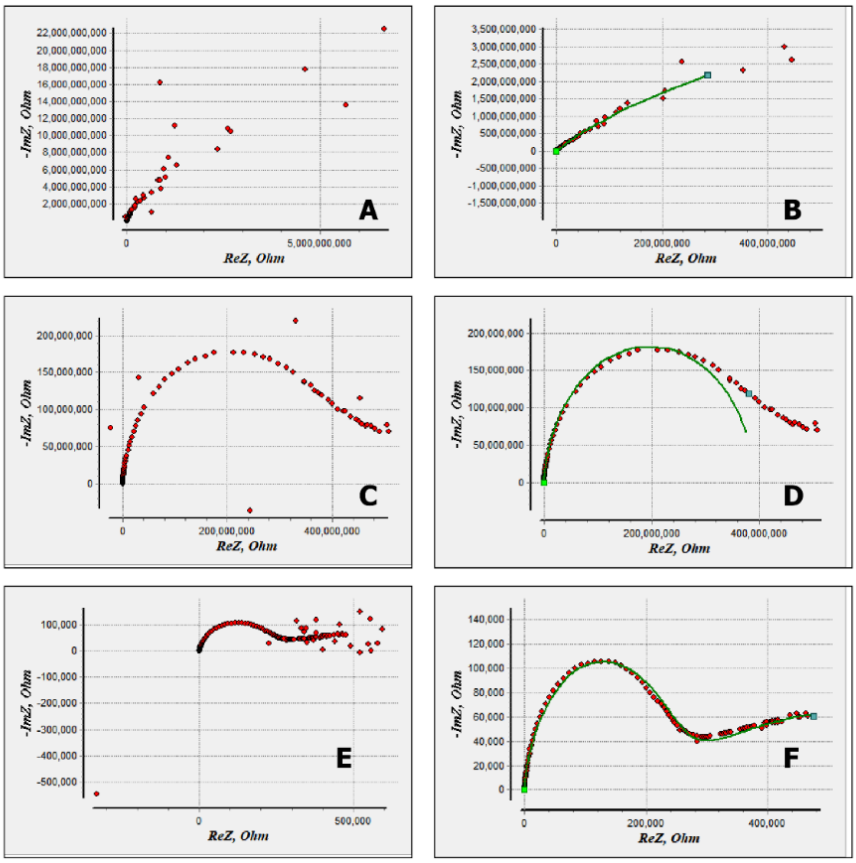

*Figure 20 - EIS argand plots **A**, **C** & **E** are the raw data which typify the data generally, where **B**, **D** and **F** show the data with outlying points muted and show the curve fitting process. The data quality of **A/B** typify the data acquired on all samples at temperatures < 300°C. **C/D** typify data gathered between 300°C and 600°C. **E/F** typify data 700°C or grater.*

There are also errors associated with the curve fitting process (Figure 21). This error is the misfit percentage between the modelled curve and the real and imaginary components of the impedance data. Note that there is a significant jump in the error below 300°C. Low temperature conductivity data are well known for being difficult to constrain.

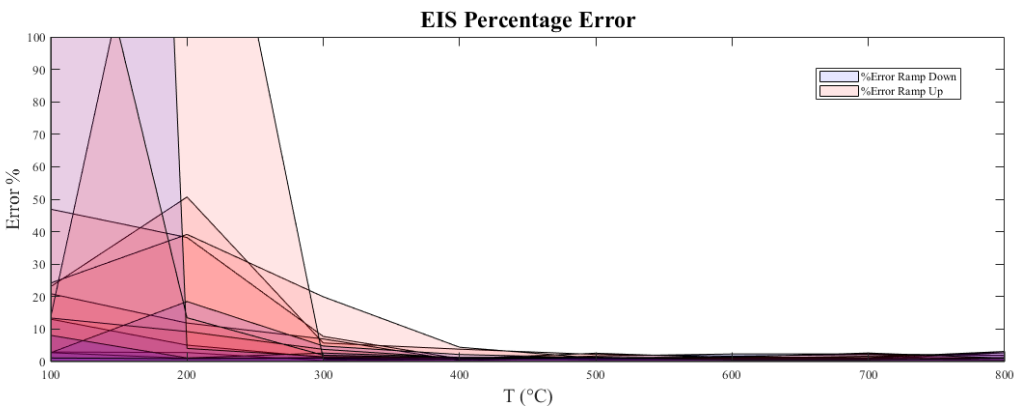

Figure 21 - The percentage error associated with the curve fitting process. This error is the percentage misfit associated with the modelled curve related to the real and imaginary components of the impedance data.

4.2.1 Conductivity Values

The calculated conductivity values for all samples is plotted in Figure 22. Triangles pointing up are measured when temperature is increasing and those pointing down are when it is decreasing.

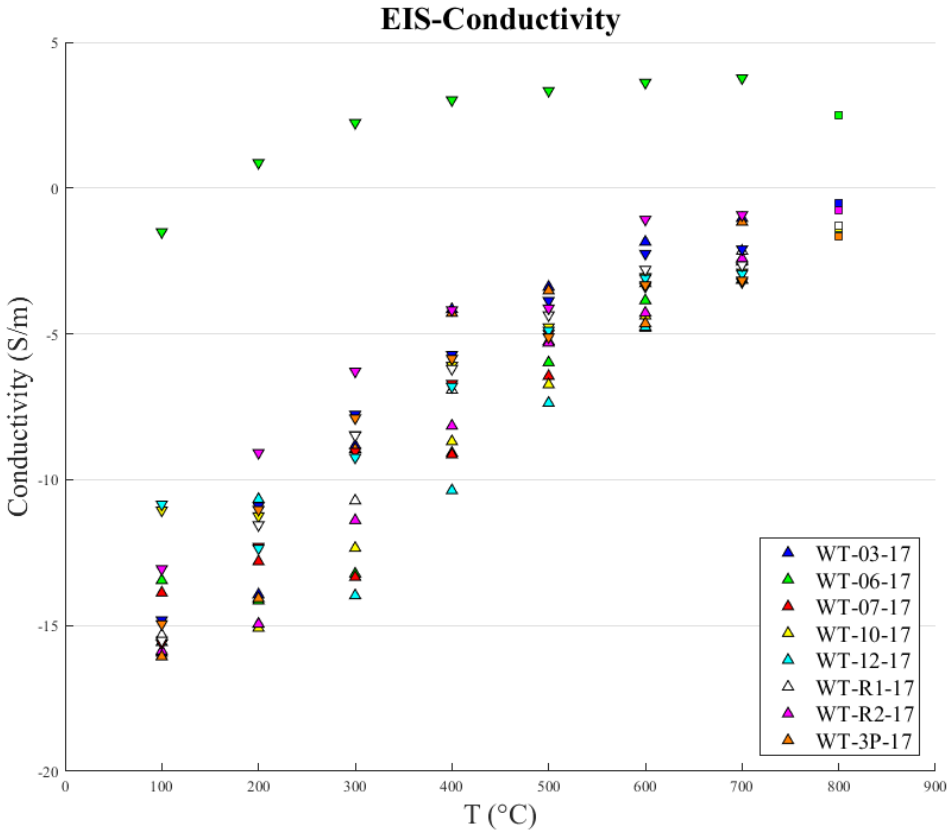

Figure 22 – Shows the conductivity *as a plot against temperature. The colours indicate the different samples and the arrow indicates if the sample measurement were taken on the ramp up (triangle up) or the ramp down (triangle down).*

A quick overview of Figure 22 shows that there is one outlier WT-06-17. An additional sample was prepared from the same rock, and was cycled twice from 100°C – 800°C and back. These were then compared and plotted as WT-R1-17 and WT-R2-17, where the repeats behaved similarly to all other samples processed. This confirmed that WT-06-17 had failed on ramp down, shown by the significant increase in the conductivity. It is likely that some type of short occurred, causing the original outlier (Figure 23)(WT-06-17). These samples also show the variance of values which, in the case of R1 and R2, can arise from a single sample. Excluding the outlier, the conductivity ranges from 10^{-4} to 10^{-9} S/m.

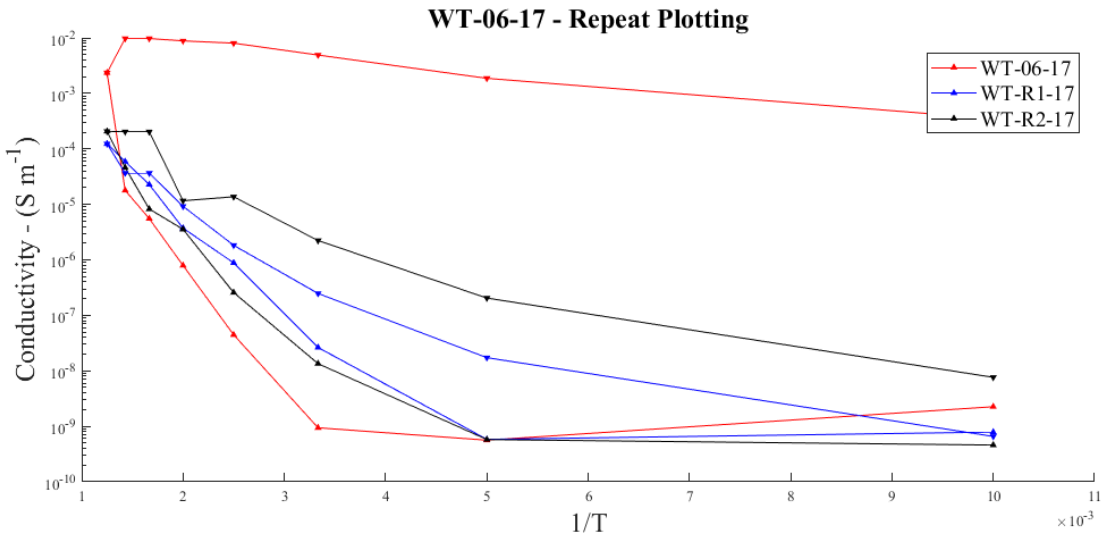

Figure 23 – Arrhenius plot comparing the WT-06-17 repeats. Note the similar ramp up behaviour of all three runs, and the anomalous ramp down of the original run WT-06-17.

4.2.2 Conductivity Mechanisms

The conductive anisotropy of the samples I was testing is also interesting. Sample WT-03-17 was the only sample which was analysed in multiple orientations. Figure 24 plots the conductivity of sample WT-03-17 (red) which was measured with the lineation of the rock against sample WT-3P-17 (blue) which was measured across the lineation. The results of Figure 24 show a higher conductivity value when current is applied with the lineation of the rock and a lower conductivity when the current is applied across it. Whilst this would indicate that the two samples display some anisotropy, the variation in conductivity measured during repeat runs of sample WT-06-17 (Figure 23) means that I cannot say this with certainty as it falls within the variance of a single sample. This indicates that if there is any anisotropy I cannot be confident that I am resolving it.

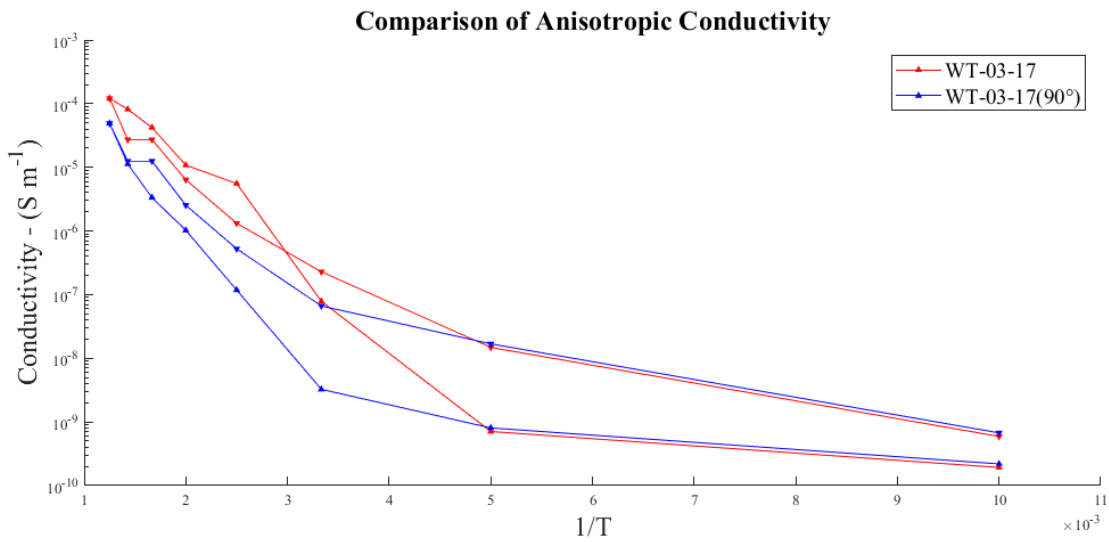

Figure 24 - Arrhenius plot comparing WT-03-17 and WT-03-17(90°). The sample which goes with the lineation has consistently higher conductivity at temperatures >200°C

Despite the calculated conductivity values being relatively similar in Figure 24, Figure 25 shows the Argand plots of 03 **A** and 3P **B** at 400°C on the ramp up. Combining the conductivity values in Figure 24 and the conductivity mechanisms visualised in Figure 25, allows for an interesting observation. Whilst the perceived conductivity value does not vary significantly with orientation relative to the lineation, the mechanisms for conduction can change. It is possible that Figure 25 B is imaging the same mechanism but as the primary mechanism is not being saturated, there is no overflow into the second mechanism with the higher activation energy. This highlights the challenges of constraining conductivity at ambient pressures.

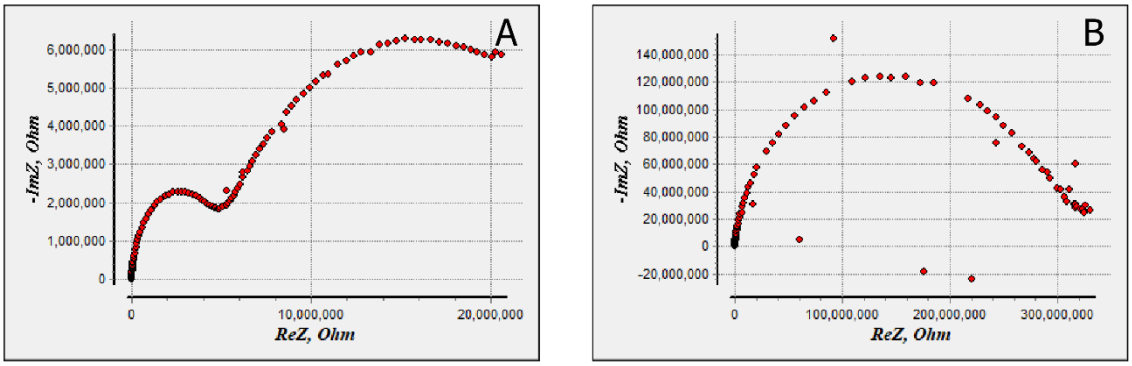

*Figure 25 - Comparison of the raw Argand plots at 400°C on the ramp up for WT-03-17 (**A**) and WT-3P-17 (**B**). Whilst the calculated conductivity value has not significantly changed, these plots imply the conductivity mechanisms have.*

A colour change occurred with all samples post EIS (Figure 26), which is likely caused by the temperature change the samples experience during the EIS analysis. XRF analysis of these two disks did not reveal any significant compositional change though XRF has limitations when identifying lighter elements. This leaves the possibility that light elements may have been removed in the form of volatiles though I cannot confirm this.

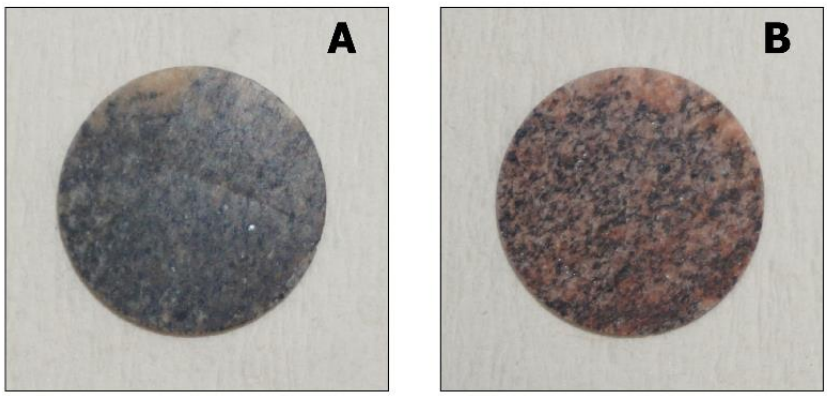

*Figure 26 -Photograph showing a sample pre (**A**) and post (**B**) EIS analysis.*

Figure 27 plots only temperatures >300°C and replaces the failed reading WT-06-17 with WT-R1-17. When comparing the increasing and decreasing temperatures there is evidence of the heating having a homogenising effect. The difference in temperatures between the lab (100-800°C) and field results at depth(<200°C) contributes to conductivity variation observed between lab and field techniques. I do not expect the natural geotherm to reach 800°C at the depths I am investigating. Therefore, higher temperature lab results should be less representative of the rocks behaviour in situ. Figure 27 also shows that heating may be removing naturally existing conductivity variations based on the homogenising trend.

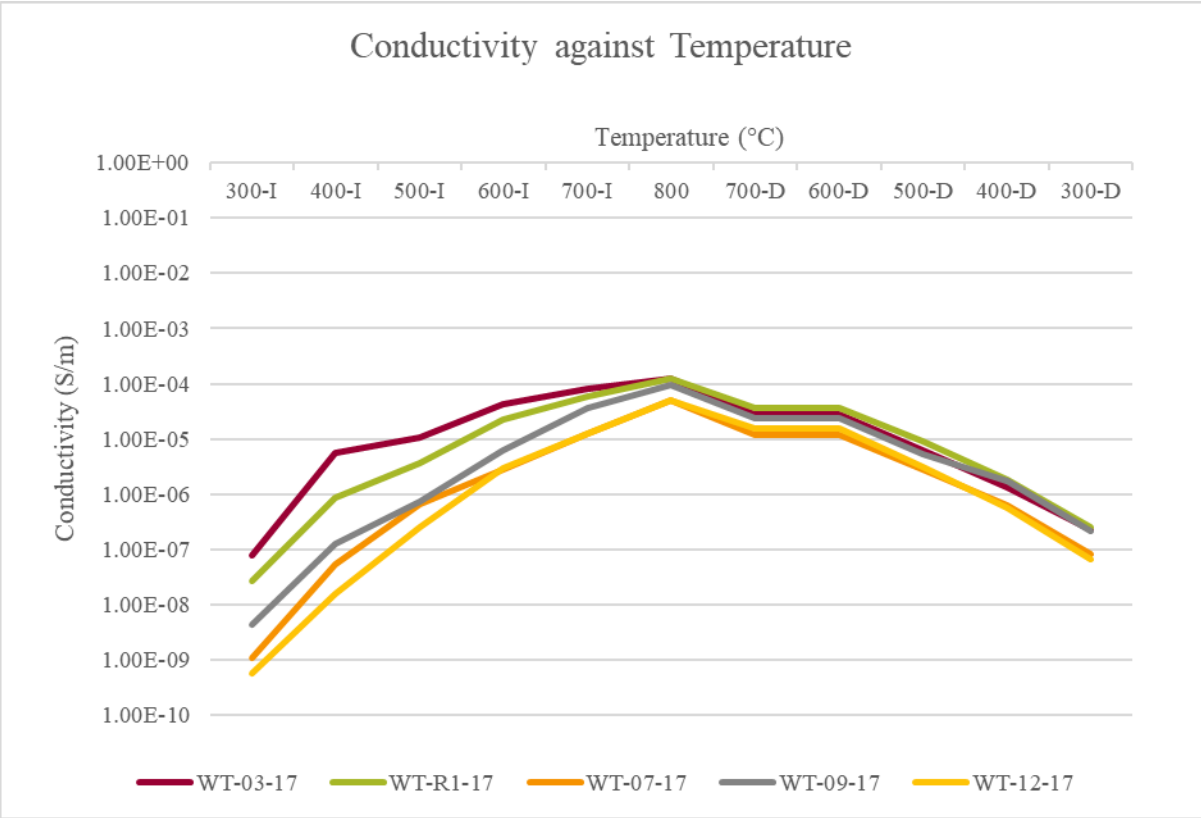

Figure 27 - Conductivity change ramp up v ramp down comparison.

4.3 TEM

4.3.1 Decay Analysis

My TEM data went through multiple stages of post processing to remove errors associated with its acquisition. The decays are plotted in Figure 28. This started in Maxwell, an EM processing software, where I initially screened the data for issues. Primarily it was revealed that the first 6-7 channel times were saturated and the following few channels had negative values. The early channels were ignored in all subsequent processing as they were measuring the primary field known as turn on transients. Due to the remote nature of this work, the early negative values are unlikely to be associated with any cultural features (electric fences, power lines). It is possible that these negatives were associated with the effect of super paramagnetic material in the lateritic soil (Buselli, 1982). The survey area is rich in iron, as was shown by the XRF analysis. I rejected these negatives from further analysis.

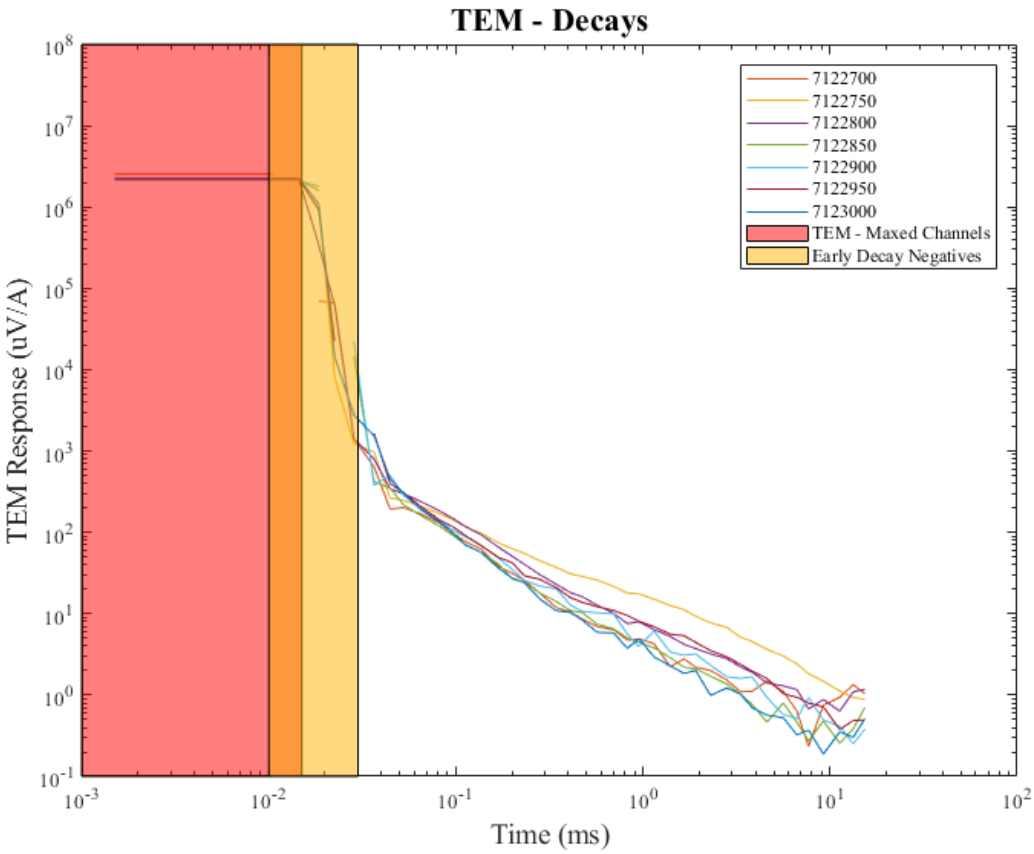

Figure 28 - TEM decays illustrating saturated channels and breaks in the decays where negative channels were removed. Where each decay is labelled by the northing on which that station was acquired.

4.3.2 Resistivity Depth Inversion

I then used the data to perform a conductivity depth inversion (CDI) using EMax, which is a plugin for Maxwell (Fullagar and Reid, 1992). I then converted the CDI solution to resistivity values and gridded the data in Matlab (Figure 29). I used a natural neighbour interpolation method

built into Matlab to interpolate the points and display the data. The geometry of the features in Figure 29 do not correlate with the expected geometry based on the structure of the shear zone. In the TEM the most conductive feature is between 80-100 Ohm m and its cause is likely the conductive cover. I then resolve a resistive feature which is continuous across the 100-130 m depth range, with a resistivity value of between 350-420 Ohm m. This gives way to a conductor at depth. This deep conductor found at depths greater than 150 m is calculated from late channel values where the signal is weakest.

It should be noted that the resistivity values measured in the TEM are orders of magnitude less resistive than those imaged by the EIS. It should also be noted that the high resistivity value on station 7122650, which was the only station done with less stacks. This may explain its' strange solutions is the cause of the strange interpolation feature imaged between station 7122650-7122700.

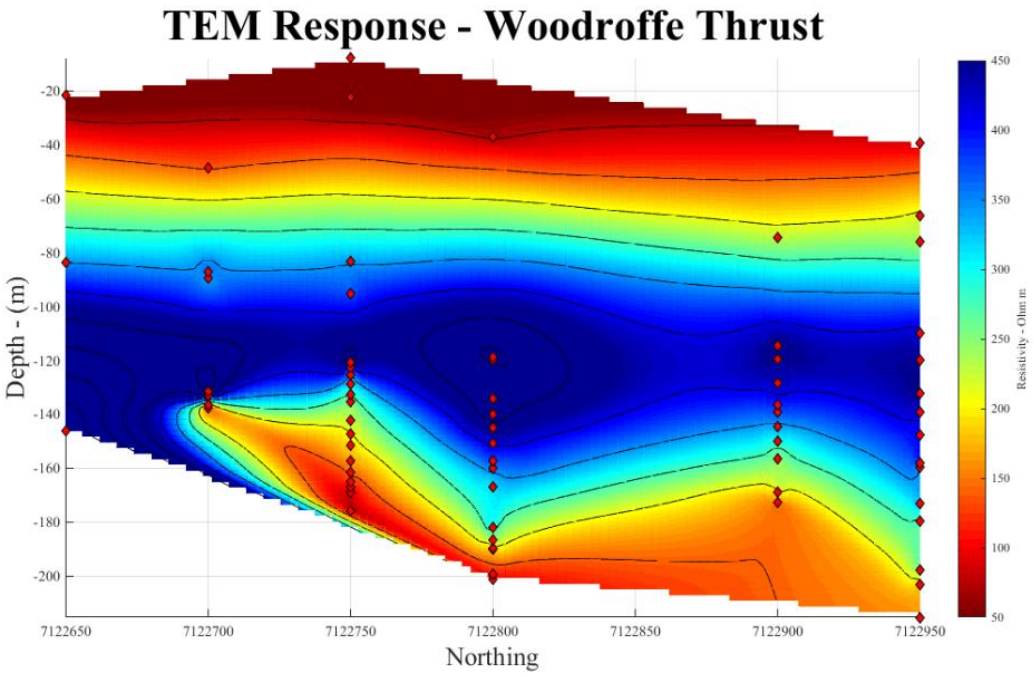

Figure 29 - Conductivity Depth Inversion of the 2150 Line. The diamonds are points at which EMax has found a conductivity solution, there are less points than one might expect due to the issues highlighted by Figure 28.

In an alternative processing of the same dataset I muted the first 9 channels which contain values which are difficult for eMax to process due to the way the software handles negatives. eMax assumes that the signal decays monotonically, so when the decays have a spike associated with noise, some of the associated decay channels are muted. Importantly, the only change is the number of solutions not the values Figure 30.

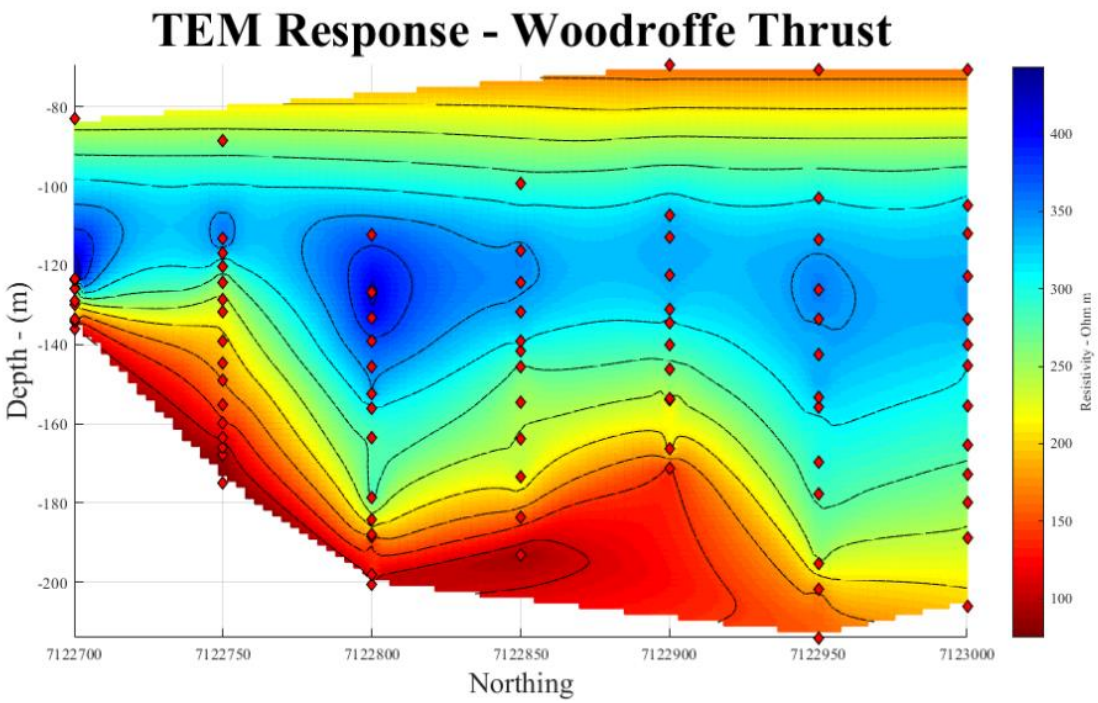

Figure 30 – Conductivity depth inversion plotted as resistivity. By muting early channel readings, it was possible to get a better distribution of solutions at depth and even on 71223000 which previously had shown no results.

4.4 MT

4.4.1 Resistivity and Phase Curves

The MT data for the stations on line 2150 are plotted in Figure 31 with the TE and TM apparent resistivity (ρ_a) and phase plots. These data were pre-processed by Selway *et al.*, (2012) using a bounded-influence remote reference MT response method (Chave and Thomson, 2004). This processing resulted in the phase and ρ_a data used in this work. If the data were not affected by static shift, there would be little vertical offset between the stations ρ_a values at longer periods. This is particularly true for stations as closely spaced as this.

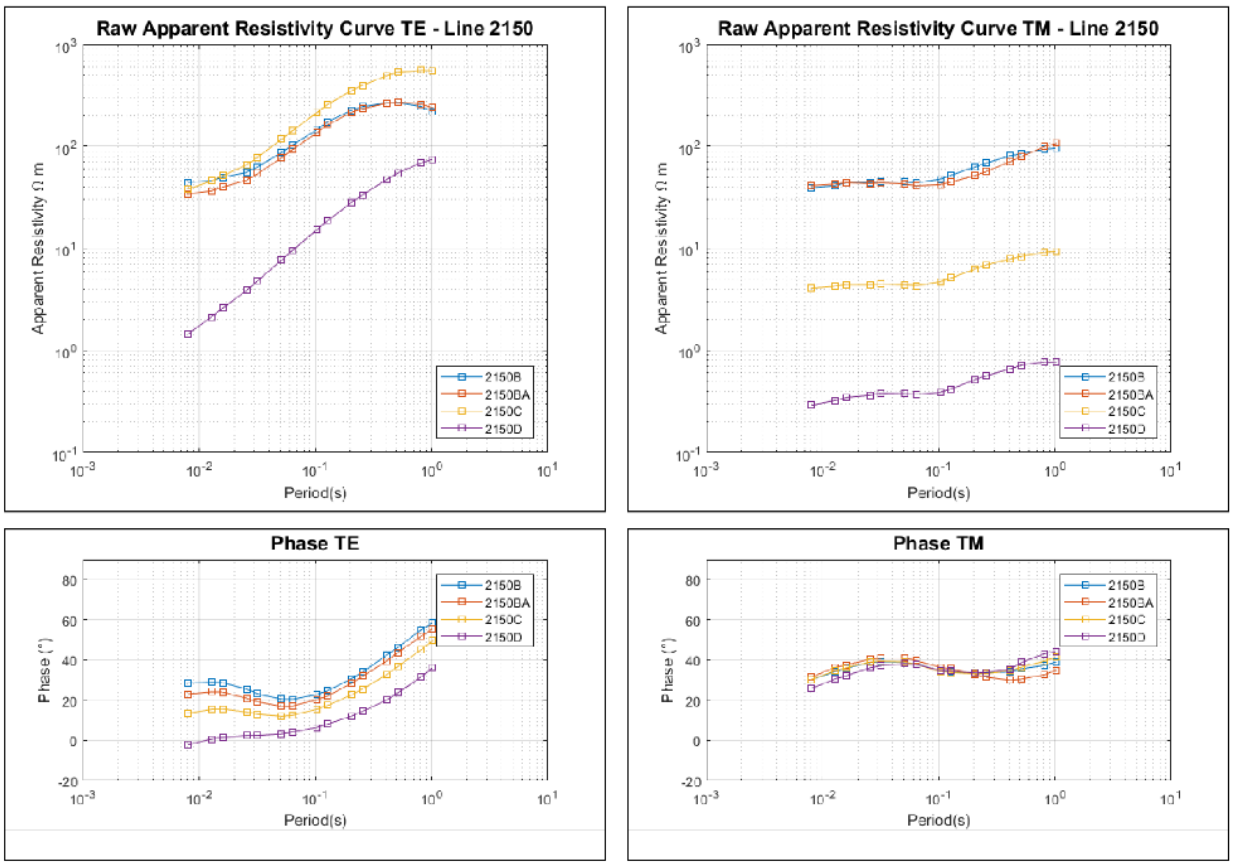

Figure 31 - MT field data showing the static shift commonly encountered in MT data. Stations are in lettered order with 2150B being the southernmost station where 2150D is the northernmost.

4.4.2 Forward Model and Static Shift Correction

TEM soundings can be used to correct for static shift errors in MT data as the magnetic field observed in TEM is relatively unaffected by surface inhomogeneities (Sternberg et. al., 1988; Pellerin, 1990). The TEM conductivity depth solutions were used to produce a 1D forward model of station 7122950 (Figure 32). This model was produced in MARED2EM (Key, 2016) to give an apparent resistivity curve (blue) to correct MT station 2150B (red) (Figure 33).

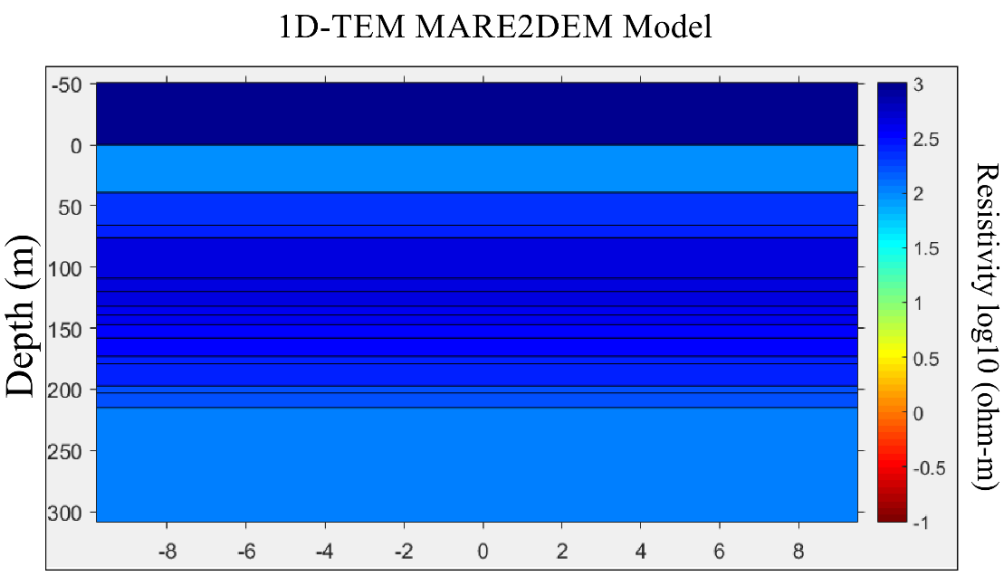

Figure 32 - 1D model created using CDI solution at station 7122950. The depth and resistivity values are based on those in Figure 29 and the horizontal extents approach infinity.

To perform the static shift correction, I correlated the longest period TEM data with the shortest period MT data and the ratio between the ρ_a at those periods was used to calculate the static correction factor. This factor was then multiplied by the apparent resistivity for each period at the station to be corrected (2150B). The result is the statically shifted line 2150B SSC (green) (Figure 33).

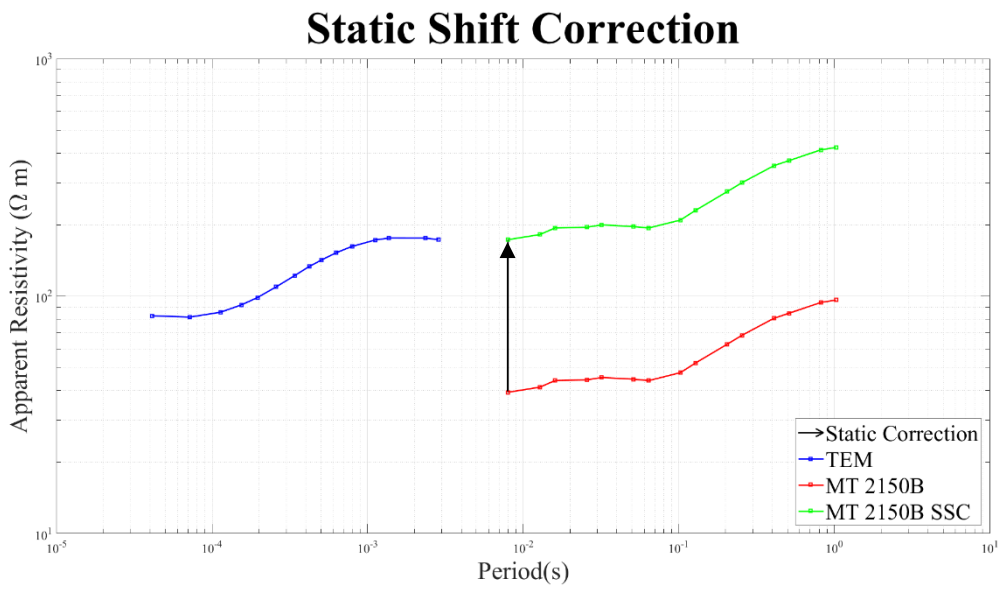

Figure 33 - Figure showing how the MT station was corrected. The arrow indicates the shift between 2150B to correlate its short period data with the long period data of the TEM dataset.

4.4.3 Resistivity Inversion

This corrected MT station was then integrated into a new MT transect containing 2150B SSC and the three other stations as processed by Selway *et al.*, (2012). This was then inverted using MARE2DEM to create a two-dimensional model oriented along the transect (Figure 34). The model used a 5% error floor and allowed for the remaining non-corrected stations to be static shifted by an inbuilt functionality within MARE2DEM. The model started using a uniform 100 Ohm m half space and a highly resistive 10^{12} layer at the surface, simulating the resistivity of air. The resulting model is plotted in Figure 34 with a RMS of 1.3519%.

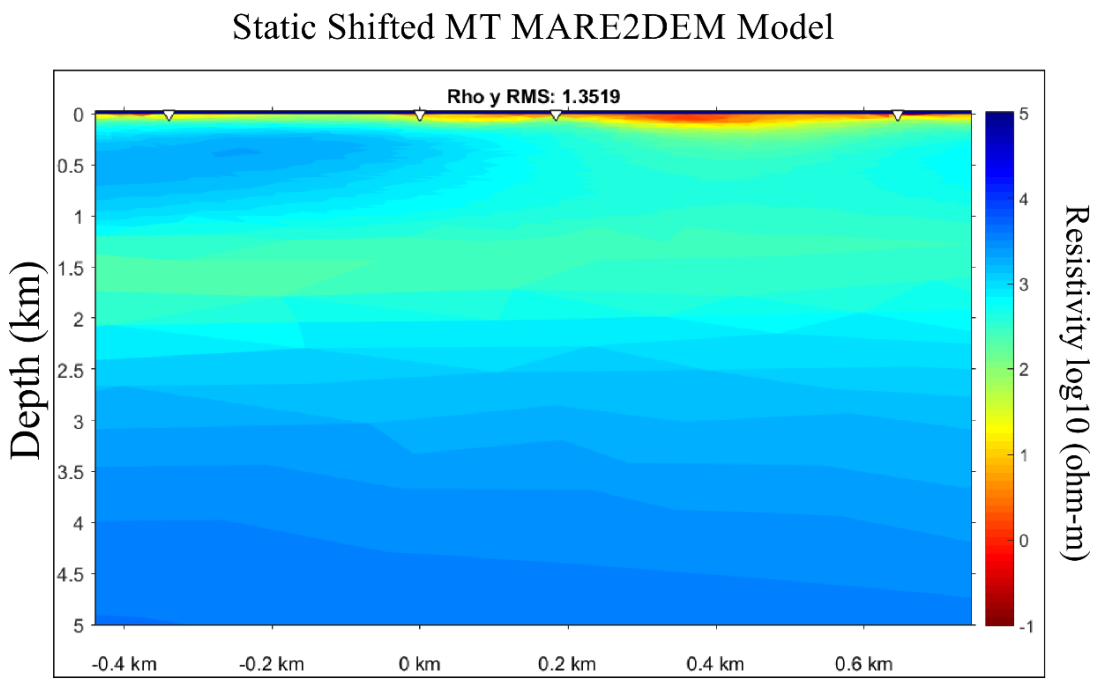

Figure 34 – Static shift corrected MT data shows a thickening of a conductive near surface layer heading north.

The model of my MT data in Figure 34 plots to 5 km depth. There is a thickening conductivity feature noted in (Selway *et al.*, 2012), which is likely associated with increasing cover heading north away from the central shear. The resistivity value associated with the cover (< 100 m) ~ 1.5 Ohm m, while at increasing depth (< 0.5 km) the resistivity values reach 340 Ohm m, a diffuse conductor at a depth of 1.5 km is ~240 Ohm m and at greater depth (>2 km) the resistivity reaches > 1000 Ohm m.

Due to the notable contrast between the EIS resistivity [10^4-10^9(Ohm m)] values and those identified in the field techniques [MT 10^{-1}-10^4 (Ohm m) & TEM 10^2-10^3 (Ohm m)]. It was decided to evaluate the ability of the MT to resolve a resistor on the scale of those found in the EIS measurements. As such, several models were run with a highly resistive body at a constant thickness (100 m) but with varied resistivity values set as follows [10^8, 10^7, 10^6, 10^5, 10^4, 10^3 Ohm-

m]. Whilst all models show relatively little variance in their apparent resistivity curves when the highly resistive body is added all show a drastic shift to their phase curves; an example is plotted in Figure 35. From this I conclude that it would be possible to resolve such a feature from the MT data if it was present.

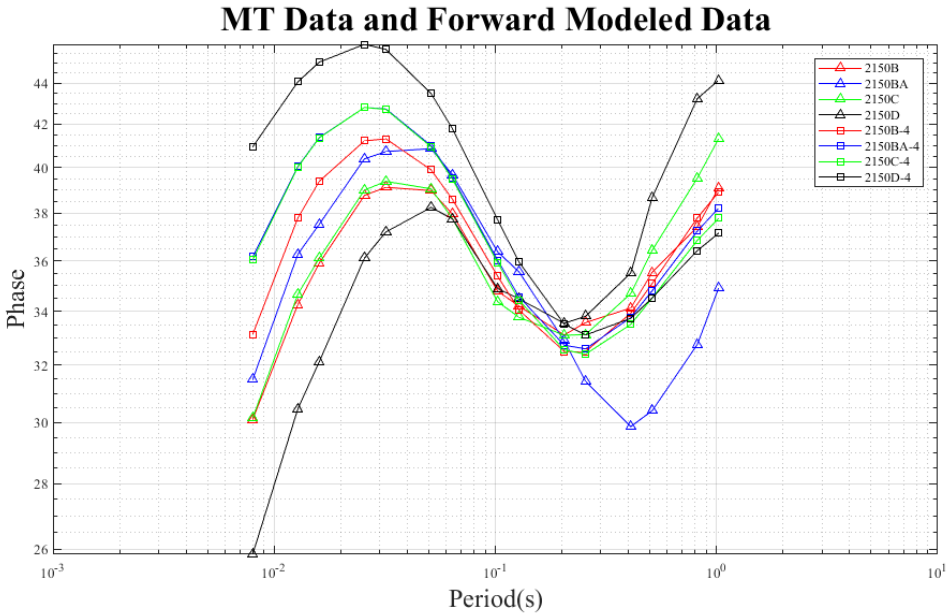

Figure 35 – The phase change in the TM mode when a resistive layer is added corresponding to the values obtained in the EIS measurements. Lines marked with triangles show the phase as observed and those marked with squares correspond to the forward modelled data where a 10^8 Ohm-m resistor was added in place of the resistive body identified in the MT between 250 m and 1 km.

5 Discussion

5.1 Overview

Shear zones are exceptionally complicated parts of the crust and this complexity impedes insightful understanding of their electrical expression. Currently there is a diverse analysis of the electrical properties of shear zones around the world. However, this analysis does not conform to a single model explaining their surface expression. The conductivity mechanisms of a given shear zone remain largely unconstrained. The results revealed by this work highlight how difficult it can be to reach a constrained understanding of the electrical properties of a shear zone due to the diverse range of techniques required. My investigation of a resistive shear (Woodroffe Thrust, NT) has allowed me to eliminate factors which have been theorised to impact the conductivity of a shear zone.

In this study, my analysis of conductivity was completed using lab and field techniques. This was done to provide a detailed understanding of both the conductivity values and the mechanisms of conduction, resulting in two key findings: i) Primarily there is no inherent property of a shear zone that means it should be conductive, ii) Secondly grainsize has no discernible impact on conductivity values of consolidated rock in upper crustal settings. A lesser finding of this work is the potential anisotropy of conductivity mechanisms with an observed change in conductivity values. I also encountered an issue prevalent to many conductivity studies, the disparity between lab and field results.

5.2 No correlation between grain size and conductivity

Trend analysis was completed by plotting the heating and cooling ramps and their associated conductivity values against the variable of interest (Percentage of grains 0.1-1 mm, Percentage of Quartz, etc.)(Figure 36), as I do not expect larger grains to impact on conductivity (Yang and Heidelbach, 2012), these plots show only the 0.1-1 mm and 1-3 mm brackets. Note that there is no clear change in conductivity with an increasing percentage of fine grains at any temperature, with each series effectively forming a horizontal line.

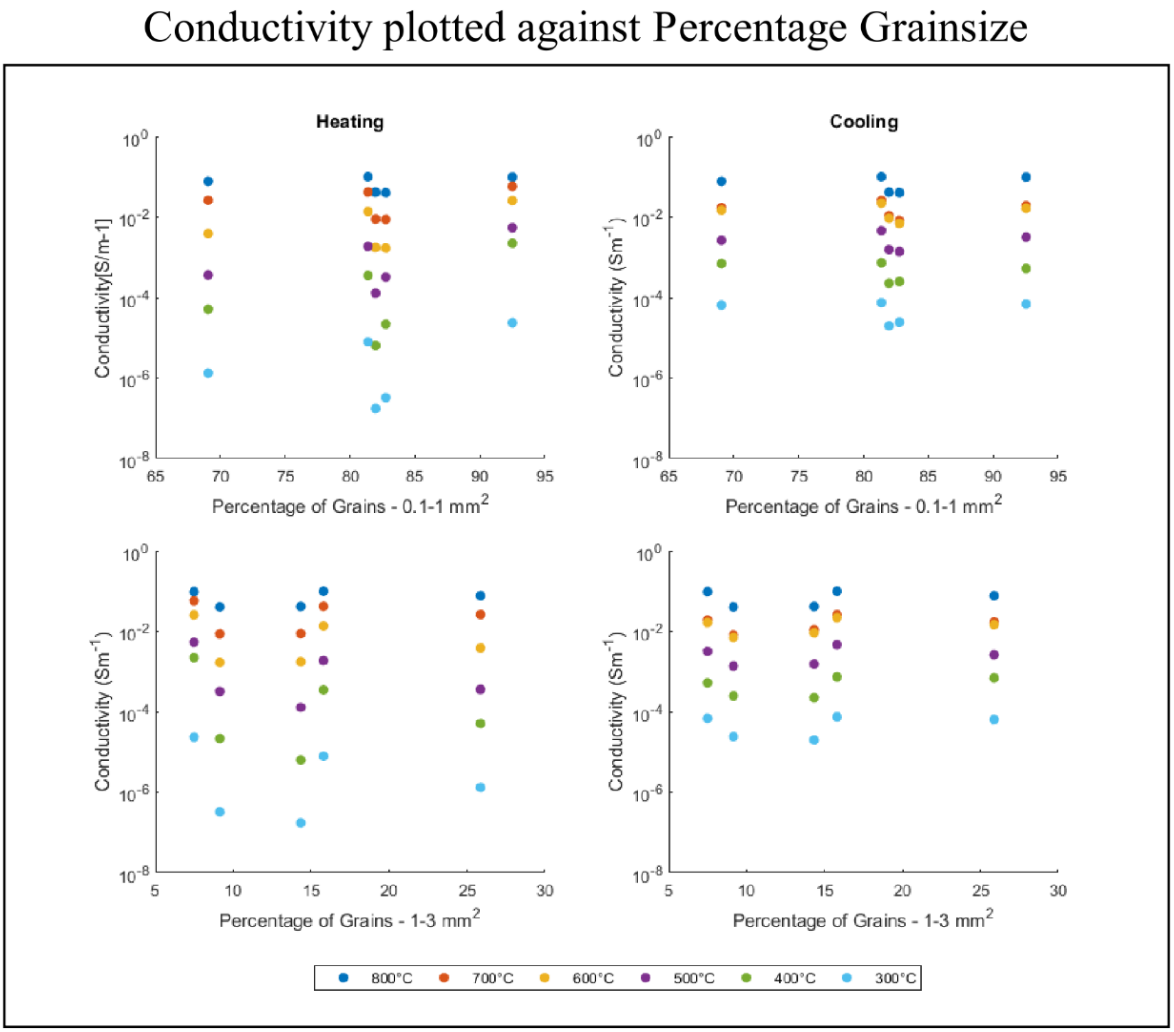

Figure 36 - Plot showing the conductivity Figure 22of the heating and cooling runs plotted against the percentage of grains in grainsize thresholds.

The limitations of the grain size characterisation now have a more profound significance. As was noted I was unable to characterise grains smaller than 0.1 mm due to the resolution. However, I found that in all samples this finest grain threshold corresponded to greater than 60% of the area. It is not much of a leap to theorise that the grains I have been unable to resolve may be quite numerous. Therefore, drawing conclusions about the effect of grainsize on conductivity from the data provided becomes less certain. The fact that I see no clear association between grain size and conductivity does agree with other results pertaining to the impact of grainsize on conductivity of clinopyroxene (Yang and Heidelbach, 2012). Their work however is on homogenous samples and diffusion based controls on conduction which is not applicable to the depth conditions my work considers.

Furthermore, analysis on the dominant mineralogy (quartz and feldspar, Figure 37), also reveals no clear trends. It is possible that the relatively low density of samples which received EIS analysis is precluding trends. However, from the evidence available I can conclude that slight compositional gradients and grainsize changes do not have a clear impact on conductivity as observed by EIS.

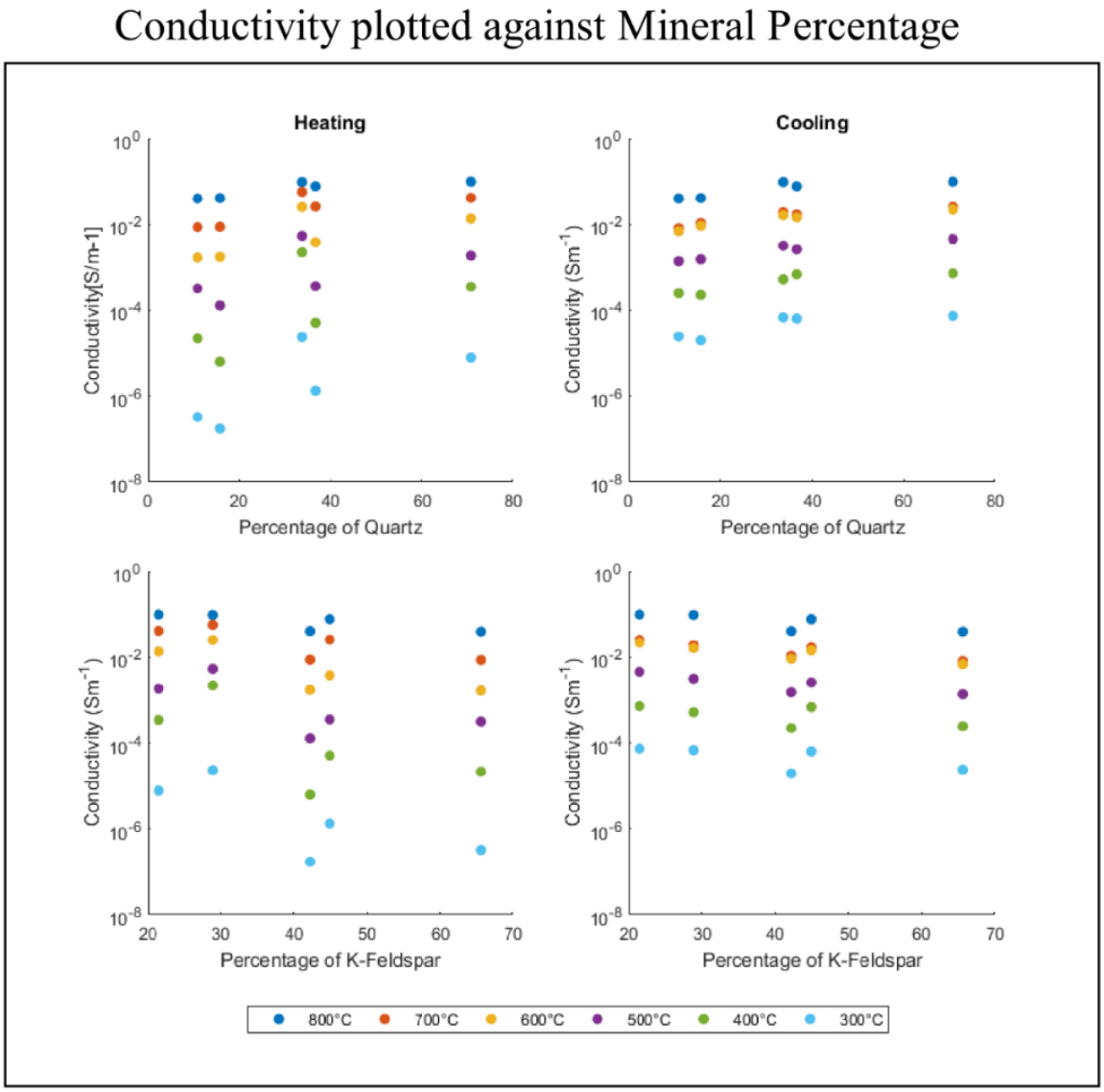

Figure 37 – Conductivity of the heating and cooling runs plotted against the percentage minerals from Figure 15.

When evaluating trends in the geophysics it is most useful to examine the TEM. This is because the MT data has a relatively low resolution (~250-500 m) when compared to the TEM (~50 m), and more so when compared to the sample acquisition (~25 m). Considering the features revealed in the TEM (Figure 29 & Figure 30) I see no clear change in conductivity with horizontal

displacement. The TEM instead shows most change in conductivity with depth. This precludes the meaningful correlation/trend analysis when considered against surface samples.

Based on the results of my lab and field analysis there is no association between grain size and conductivity in this setting. I also see no evidence for any consistent trends associated with the compositional gradients and the EIS results.

5.2.1 Associated findings - Potential Anisotropy of Mechanisms

An interesting feature of the data is the potential observation of different conductivity mechanisms between the two different orientations of the electrochemical impedance spectroscopy (EIS) data. There is not great evidence for an overall change in the conductivity value between the two orientations. However, the Argand plots in Figure 24 seem to display two distinct curves which would arise from different conductivity mechanisms.

This implies that whilst a medium may not appear anisotropic in conductivity value, it is anisotropic in its mechanisms. However, this conclusion comes with so many caveats that it is far from conclusive. Primarily this is a single data point and this feature is observed in no other sample. It has been shown that anisotropy can arise from a relatively slight increase in the directionality of the associated conductive pathway. Consider for example the case of cracks hosting water. To see anisotropy in this setting with a factor of 10 between the two orientations on a field scale, does not require 10 times as many cracks in one direction than the other (Bahr 1997). The addition of any anisotropy would result in larger scale features in the geophysics, which ultimately, it does not. The identification of these mechanisms is interesting, but it does not correlate to a larger feature in the geophysics.

Alternatively, if I do choose to accept the possibility of anisotropic conductivity mechanisms, one possible explanation could be the iron rich films imaged in the XRF. It is possible for elevated iron content to increase conductivity in olivine (Yoshino *et al.*, 2012) and the ability of grain boundary films to conduct is proportional to how interconnected they are (Pous *et al.*, 2004). It is therefore reasonable to assume that if you sample such that the Fe rich phases in Figure 17 are predominately along the lineation of the rock, they will remain intact and could act as a viable alternative conduction pathway. Whereas if you sampled across the lineation of the rock, breaking most of the conduction pathways, you would reduce the number of potential mechanisms at play. The next crucial step would be to repeat the EIS analysis to confirm the presence of the supposed anisotropy. Given the lack of evidence I cannot confirm the existence of the effect described above. However, it is an interesting notion that the conductivity value could be indistinguishable in different orientations, but the mechanisms of conduction would change.

5.3 Shears are not inherently conductive

The other main conclusion of my work is that shears are not inherently conductive. Based on the results of my lab and field analysis there is no inherent property of a shear zone which makes it conductive. Using conductivity values derived from multiple methods (EIS, MT and TEM) no results reveal anomalously conductive behaviour when compared to equivalent results on similar materials and settings. The high resistivity of my results typify the Woodroffe thrust as being a prime example of a resistive shear.

The common explanation for conductivity anomalies has been the presence of some highly conductive material mixed in a relatively resistive silicate matrix (Shankland and Ander, 1983). Examples of these anomalous conductors include: water, partial melt, hydrated minerals (including clays), magnetic oxides, graphite, and sulphides. Based on the tectonic setting I do not expect any melt. Vernon *et al.*, (1995) noted the anhydrous nature of the rocks in the survey area. My XRF data does not reveal any extensive amounts of sulphur but are unable to accurately resolve light elements such as the carbon found in graphite. Hence, I do not expect a mineralogical source of conductivity, such as sulphur or hydrated minerals. However, I am unable to rule out the presence of graphite based on the XRF alone.

The role of fluids like saline water is more difficult to constrain. The area has been drilled intermittently as far back as the 1958 until present, mainly for stock and domestic watering (Australian Government: Bureau of Meteorology, 2017). However, most drill holes in the survey area were abandoned during construction or did not encounter water. The nearest bore which did was 5 km from the nearest MT station (Supp.Figure 5). Moreover, these drill holes only reach depths of between 30-80 m, which makes it difficult to further constrain the presence of water at depth. Given the evidence it is unlikely that I would encounter fluids in the upper 80 m.

In the TEM the features were: cover (~80-100 Ohm m), a resistive layer (~350-420 Ohm m) and deep conductor (~100 Ohm m). It is possible that the conductor at depth could be saline water. However, the drilling information above does not reach depths which could confirm this. Work using TEM to map ground water found that fresh water was ~100 Ohm m and saline water gave values <5 Ohm m (Kafri and Goldman, 2005; Rajab and El-Naqa, 2013). Based on this it is likely that if the conductor at depth is fluids, they are not saline. Results of the MT were similarly resistive the strongest resistor was beneath stations 2150B and 2150 BA. It is approximately three times the resistivity (1100 Ohm m) of the surrounding values (350 Ohm m), and its cause is unknown. What is important to note is that if you set aside the thickening cover to the north of the TEM stations the MT confirms the relatively high overall resistivity of this shear zone.

Compare these values to the San Andreas Fault (SAF) where the central shear has a resistivity value of 1-10 Ohm m from surface all the way to 3 km depth (Unsworth *et al.*, 1997). By

comparison the Woodroffe Thrust is highly resistive. This result falls in line with my understanding of the mechanisms of conduction at play in a crustal shear setting. As discussed damaged zones allow for lower resistivity values via the ingress of the pore fluid. This work's setting has a lack of any clear damaged zone. The area also lacks an active or clear fluid source as was the case in the more conductive shears (SAF). The mineralogy of the area is also anhydrous with no obvious conductive minerals or structures.

Interpreting my lab results is challenging as most of the conductivity analysis done on geological samples focuses on high pressure experiments typically targeting conditions in the lower crust or upper mantle. My most conductive results at 800°C are 10^{-4} S/m and these agree roughly with mineralogical conductivities of quartz (10^{-2} S/m) and K-feldspar (10^{-4} S/m) (Bagdassarov and Delépine, 2004; Yang *et al.*, 2012). These values are more resistive compared with results where graphite films are present (~50 S/m) (Jödicke *et al.*, 2004). Alternative experimental techniques soak the sample in brine to simulate an interconnected pore fluid network (Stesky, 1986; Glover and J., 1994). This increases the conductivity, but results remain several orders of magnitude too small to explain observed field data. Furthermore, in my setting I do not expect a damaged zone, and the associated interconnected network of fluid filled cracks. My EIS results also show no unambiguous evidence relating conductivity to volatiles lost. As there is no systematic decrease in conductivity on the ramp down after volatiles should have been lost.

Ultimately my lab results conform well with other lab based conductivity results. It should also be considered that these conductivity values are being acquired at temperatures up to 800°C. This is much higher than I would expect at near surface depths, such as those investigated in this work. It is unlikely in non-volcanic settings to encounter temperatures greater than 200°C in the upper 10 km. My deepest values approach 5 km using the MT data.

Data repeatability is a real concern for the EIS measurements. Constraints on time and resources meant that no standard was evaluated, and I was unable to complete repeat readings across my samples. Both these measures would have increased the reliability of my data. The analysis of WT-06-17 (R1 and R2) hints at the variance within a single sample. This variation and the data repeatability stem from the nature of data analysis of impedance spectroscopy. Assessing the background resistivity of the unit is another test I was unable to run (Yang *et al.*, 2011).

The data analysis required to get the physical properties out of a EIS measurement is cumbersome (Macdonald and Johnson, 2005). There is also no standardised and simplistic way to propagate errors through. Therefore, I have a result matching the literature but with minimal information as to its reliability. The only error information associated with the EIS data is the percent error on the curve fitting. This does little to constrain errors between points and simply

shows that lower temperature results are less reliable. Moreover, modelling of the equivalent circuit was based on previous work (Lanati, 2016). Ideally the equivalent circuit would be designed after developing a plausible physical model for my setting, testing this model mathematically and then performing a curve fitting (Macdonald and Johnson, 2005). This was unfortunately not viable due to time constraints.

There are several limitations inherently associated with the field techniques used in this work and the subsequent data reduction (Lienert *et al.*, 1980; McNeill, 1980; Nabighian and Corbett, 1991; Simpson and Bahr, 2005). Issues such as limited dynamic range, long term repeatability of values and galvanic distortion are all common and well documented. Specifically encountered in my TEM data are the saturated early channel values and early decay negatives. Potential causes for these issues have already been identified in the results. However, the impacts on interpretation are clear with the near surface data (<80 m depth) having low resolution, obscuring the near surface, and limiting my ability to understand its conductivity. This issue likely stems from the timing windows chosen during acquisition. The timing used placed emphases on later decay times and this allowed for a greater resolution at depth. This was important for viable static shift corrections to the MT data. TEM data were processed using proprietary software such as Maxwell and eMax (Fullagar, 1989; Fullagar and Reid, 1992; Reid *et al.*, 2006). The user is allowed input at different steps, screening the data, checking channel times, and muting erroneous values. Due to the time constraints on the project, data handling went unseen, hidden within a 'black box'. Not knowing how values are handled when null or non-monotonically decreasing, limits my ability to discuss my results in a more in-depth fashion.

In this work I encountered and experimented with overcoming an example of galvanic distortion (static shift) in magnetotellurics data. My attempts though only partially used for the outcome of this work gave me insight into how they could be tackled. Fortunately, the static shift was minimal and easy to correct for by using the TEM data. MARE2DEM as was used primarily to build models and run inversions (Key, 2016). MARE2DEM bases its processing on Occam's inversion method (deGroot-Hedlin, 1990).

MT in the past has been thoroughly analysed at the San Andreas fault, due primarily to the enduring nature of the site's data acquisition. This enduring nature made possible long term repeatability assessments of MT data (Lienert *et al.*, 1980). The authors estimated the repeatability of their calculated apparent resistivities to be 10-20% and attributed this degree of variance to changes in the water table as well as uplift. They also noted changes in their apparent resistivity values by a factor of eight associated with rainfall and associated water in the thin soil layers. This

highlights the difficulties in assessing the repeatability of field results due to the complications associated with changing field conditions.

5.3.1 Associated findings - Disparity between Lab and Field Results

There is a clear disparity between the results of the lab and the field, which has been noted throughout this discussion. The lab resistivity values range from 10^3 Ohm m at 800°C to 10^7 Ohm m, between 100°C and 800°C. The TEM field measurements range between 80 Ohm m - 400 Ohm m. This disparity between lab and field results has been encountered before (Shankland and Ander, 1983; Bahr, 1997). This issue likely arises due to the complex process of reducing measurements taken on inhomogeneous medium, to a single numerical value. Before furthering this discussion, my primary assumption is that there exists only one true conductivity value for a given material. To elaborate, it should be possible to calculate this value regardless of what technique used. Therefore, the only explanation for any disparity is either not measuring the same material or the calculation fails to account for a variable affecting the measurement.

Historically the disparity is typically addressed by citing failures or limitations of the laboratory measurements of the sample. Either it is drier than would be expected of the earth (Stesky, 1986), the samples are non-representative of the larger geological setting (Mitchell *et al.*, 2010) or it is depleted in volatiles via the measuring process itself (Shankland and Ander, 1983). In my own work I saw a colour change in the sample which was likely attributed to the loss of volatiles which occurred as the sample was heated. The effect of volatiles has been discussed and its impact observed to be minimal. It is therefore unlikely that volatiles explain the disparity between lab and field. The other main limitation of the laboratory methods is the non-representative sampling. Due to the small sample size viable for lab methods, larger pathways for fluids or other conductive minerals may not be represented (Bahr, 1997). All data considered we can conclusively say that the Woodroffe Thrust is a resistive shear.

5.4 Future Work

This work was completed over an eight-month period in conjunction with a Master's of Research. Any project this involved and with these time constraints will be forced to forego many opportunities to improve on its conclusions for the sake of expediency. Therefore, it is possible to enrich the dataset established here with further research.

There are alternative methodologies for most tasks undergone in this project. A better classification of grainsize and mineralogy could be achieved using a higher resolution technique such as scanning electron microscopy (SEM). Identifying and constraining the composition of any grain boundary films would also be ideal, and this could be completed using electron microprobe analysis (EMPA). A proper understanding of grain boundaries presents could be gained by trialling

a novel technique which is currently being developed to image pore space and the injection of CO_2 into shales (Wang *et al.*, 2017). The use of MRI could be an interesting way to image grain boundaries in a rock and subsequently visualise and quantify the change in conduction pathways between different orientations/samples. Measuring conductivity in both a field and a lab setting could also stand improvement. More survey and lab time would be useful in reaching more assertive conclusions. A detailed analysis of error propagation method through the EIS would also be useful in constraining my values. Testing on controlled grain size samples as has been done before (Yang and Heidelbach, 2012) however it would be interesting to attempt to replicate these results using the methodology of this work. Extending the field transect across and over the ridgeline to get a symmetrical understanding of the shear would also be interesting, as we could just be imaging the resistive half of the shear (Maercklin *et al.*, 2005).

6 Conclusions

Presented in this work is my lab and field analysis over the Woodroffe Thrust (WT), Northern Territory. The primary goal of this work was understanding its electrical response and investigating the factors acting on it. Analysis revealed that the Woodroffe Thrust is a resistive shear zone. Despite observed variation in grainsize I found no consistent trend associated with the conductivity, as revealed by the lab and field analysis.

My observations on the overall resistive nature of the Woodroffe Thrust and on the disparity between lab & field measurements, both contribute to wider body of knowledge about these issues. In the case of the WT as a resistive shear, it is important to highlight that shear zones cannot be typified as a single response. A given shear zone's electrical response is proportional to its setting and contents, not to its status as a shear zone. This work has shown that to understand the electrical expression of a shear zone requires detailed analysis. When considering the disparity between lab and field results I identified the complexity of the issue and overviewed some key aspects currently undergoing review. This project's goal was to consider shear zones and their electrical expression in detail, with the larger goal of contributing to the understanding of shear zones globally. During my work I showed the steps necessary to accurately constrain shear zones. The results on the effects of grainsize show that there is no clear impact on conductivity. Also identified was the potential for anisotropic conductivity mechanisms but non-anisotropic conductivity values.

7 References

Aitken, A. R. A. *et al.* (2009) 'Constrained potential field modeling of the crustal architecture of the Musgrave Province in central Australia: Evidence for lithospheric strengthening due to crust-mantle boundary uplift', *Journal of Geophysical Research: Solid Earth*, 114(12).

Australian Government : Bureau of Meteorology (2017) *Australian Groundwater Explorer*. Available at: http://www.bom.gov.au/water/groundwater/explorer/map.shtml.

Bagdassarov, N. . and Delépine, N. (2004) 'α–β Inversion in quartz from low frequency electrical impedance spectroscopy', *Journal of Physics and Chemistry of Solids*, 65(8–9), pp. 1517–1526.

Bahr, K. (1997) 'Electrical anisotropy and Conductivity distribution functions of fractal random networks and of the crust: The scale effect of connectivity', *Geophys. J. Int.*, 130(December), pp. 649–660.

Becken, M. and Ritter, O. (2012) 'Magnetotelluric Studies at the San Andreas Fault Zone: Implications for the Role of Fluids', *Surveys in Geophysics*, 33(1), pp. 65–105.

Borden, D. and Giese, R. F. (2001) 'Baseline studies of the clay minerals society source clays: Cation exchange capacity measurements by the ammonia-electrode method', *Clays and Clay Minerals*, 49(5), pp. 444–445.

Budd, A. (2001) *Musgrave Block Synthesis*.

Buselli, G. (1982) 'The effect of near-surface superparamagnetic material on electromagnetic measurements', *Geophysics*, 47(9), pp. 1315–1324.

Cagniard, L. (1953) 'Basic Theory of the Magneto-telluric Method of Geophysical Prospecting', *Geophysics*, 18(3), pp. 605–635.

Caine, J. S., Evans, J. P. and Forster, C. B. (1996) 'Fault zone architecture and permeability', *Geology*, 24(1), pp. 1025–1028.

Camacho, A. and Fanning, C. M. (1995) 'Some isotopic constraints on the evolution of the granulite and upper amphibolite facies terranes in the eastern Musgrave Block, central Australia', *Precambrian Research*, 71(1–4), pp. 155–181.

Chakraborty, S. (2008) 'Diffusion in Solid Silicates: A Tool to Track Timescales of Processes Comes of Age', *Annual Review of Earth and Planetary Sciences*, 36(1), pp. 153–190.

Chave, A. D. and Thomson, D. J. (2004) 'Bounded influence magnetotelluric response function estimation', *Geophysical Journal International*, 157(3), pp. 988–1006.

Corseri, R. *et al.* (2017) 'Magnetotelluric evidence for massive sulphide mineralization in intruded sediments of the outer Vøring Basin, mid-Norway', *Tectonophysics*. Elsevier B.V., 706–707, pp. 196–205.

Coster, H. P. (1948) 'The Electrical Conductivity of Rocks at High Temperatures', *Geophysical Journal International*, 5(6).

deGroot-Hedlin, C. (1990) 'Occam's inversion to generate smooth, two-dimensional models from magnetotelluric data', *Geophysics*, 55(12), p. 1613.

Flude, S., Haschke, M. and Storey, M. (2016) 'Application of benchtop micro-XRF to geological materials', *Mineralogical Magazine*, pp. 1–53.

Fossen, H. and Cavalcante, G. C. G. (2017) 'Shear zones – A review', *Earth-Science Reviews*. Elsevier,

171(January), pp. 434–455.

Fullagar, P. K. (1989) 'Generation of conductivity-depth pseudo-sections from coincident loop and in-loop TEM data', *Exploration Geophysics*, 20(2), pp. 43–45.

Fullagar, P. K. and Reid, J. E. (1992) 'Conductivity-depth transformation of fixed loop TEM Data', *Exploration Geophysics*, 23(3), pp. 515–519.

Glover, P. W. J. (1996) 'Graphite and electrical conductivity in the lower continental crust: A review', *Physics and Chemistry of the Earth*, 21(4), pp. 279–287.

Glover, P. W. J. and J., V. F. (1994) 'Electrical Conductivity of the continental crust', *Geophysical Research Letters*, 21(22), pp. 2357–2360.

Grahame, D. C. (1947) 'The electrical double layer and the theory of electrocapillarity', *Chemical Reviews*, 41(3), pp. 441–501.

ten Grotenhuis, S. M. *et al.* (2004) 'Electrical properties of fine-grained olivine: Evidence for grain boundary transport', *Journal of Geophysical Research*, 109(6), pp. 1–9.

Heinson, G. and Constable, S. (1992) 'The electrical conductivity of the oceanic upper mantle', *Geophysical Journal International*, 110(1), pp. 159–179.

Jödicke, H. *et al.* (2004) 'Syngenetic, thin graphite-rich horizons in lower crustal rocks from the Serre San Bruno, Calabria (Italy), and implications for the nature of high-conducting deep crustal layers', *Physics of the Earth and Planetary Interiors*, 141(1), pp. 37–58.

Jones, A. G. and Ferguson, I. J. (2001) 'The electric Moho.', *Nature*, 409(January), pp. 331–333.

Kafri, U. and Goldman, M. (2005) 'The use of the time domain electromagnetic method to delineate saline groundwater in granular and carbonate aquifers and to evaluate their porosity', *Journal of Applied Geophysics*, 57(3), pp. 167–178.

Kanngießer, B. (2003) 'Quantification procedures in micro X-ray fluorescence analysis', *Spectrochimica Acta - Part B Atomic Spectroscopy*, 58(4), pp. 609–614.

Karato, S. *et al.* (1990) 'The role of hydrogen in the electrical conductivity of the upper mantle', *Nature*, 347(6290), pp. 272–273.

Karato, S. I. and Wang, D. (2013) 'Electrical Conductivity of Minerals and Rocks', *Physics and Chemistry of the Deep Earth*, pp. 145–182.

Katsura, T., Sato, K. and Ito, E. (1998) 'Electrical conductivity of silicate perovskite at lower-mantle conditions', *Nature*, 395(October), pp. 493–495.

Key, K. (2016) 'MARE2DEM: A 2-D inversion code for controlled-source electromagnetic and magnetotelluric data', *Geophysical Journal International*, 207(1), pp. 571–588.

Lanati, A. W. (2016) 'Possible compositional effects on the electrical conductivity of olivine : A preliminary study', *MQU Research Online*.

Lasia, A. (2002) *Electrochemical Impedance Spectroscopy and its Applications*, *Modern Aspects of Electrochemistry*.

Lienert, B. R. *et al.* (1980) 'Long Term Variations Resistivities San Andreas Fault in Magnetotelluric Observed near the in Southern Apparent California', *Journal of Geomagnetism and Geoelectricity*, pp. 757–775.

Lin, A. *et al.* (2005) 'Propagation of seismic slip from brittle to ductile crust: Evidence from

pseudotachylyte of the Woodroffe thrust, central Australia', *Tectonophysics*, 402(1–4 SPEC. ISS), pp. 21–35.

Macdonald, J. R. and Johnson, W. B. (2005) *Impedance Spectroscopy Theory, Experiment, and Applications*, *America*.

Maercklin, N. *et al.* (2005) 'Characterizing a large shear-zone with seismic and magnetotelluric methods: The case of the Dead Sea Transform', *Geophysical Research Letters*, 32(15), pp. 2–5.

McNeill, J. D. (1980) 'Electromagnetic Terrain Conductivity Measurement at Low Induction Numbers', *Technical note TN*, p. 13. Available at: http://www.geonics.com/pdfs/technicalnotes/tn6.pdf.

Mitchell, M. R. *et al.* (2010) 'Application of Impedance Spectroscopy for Determining Fabric Anisotropy of Fine-Grained Soils', *Journal of Testing and Evaluation*, 38(3), p. 102624.

Murase, T. and McBirney, A. R. (1973) 'Properties of some common igneous rocks and their melt at high temperatures', *Geological Society of America Bulletin*, 84(11), pp. 3563–3592.

Nabighian, M. N. . and Corbett, J. D. . (1991) *Electromagnetic Methods in Applied Geophysics - Part A and B*.

Nayak, P. S. and Singh, B. K. (2007) 'Instrumental characterization of clay by XRF, XRD and FTIR', *Bulletin of Materials Science*, 30(3), pp. 235–238.

Nover, G. (2005) 'Electrical properties of crustal and mantle rocks - A review of laboratory measurements and their explanation', *Surveys in Geophysics*, 26(5), pp. 593–651.

Padrón-Navarta, J. A., Hermann, J. and O'Neill, H. S. C. (2014) 'Site-specific hydrogen diffusion rates in forsterite', *Earth and Planetary Science Letters*. Elsevier B.V., 392, pp. 100–112.

Parkhomenko, E. I. (1982) 'Electrical resistivity of minerals and rocks at high temperature and pressure', *Reviews of Geophysics*, 20(2), pp. 193–218.

Pellerin, L. (1990) 'Transient electromagnetic inversion: A remedy for magnetotelluric static shifts', *Geophysics*, 55(9), p. 1242.

Pommier, A. (2014) *Interpretation of Magnetotelluric Results Using Laboratory Measurements*, *Surveys in Geophysics*.

Pous, J. *et al.* (2004) 'Electromagnetic imaging of Variscan crustal structures in SW Iberia: The role of interconnected graphite', *Earth and Planetary Science Letters*, 217(3–4), pp. 435–450.

Rajab, J. S. A. . and El-Naqa, A. R. . (2013) 'Mapping groundwater salinization using transient electromagnetic and direct current resistivity methods in Azraq Basin, Jordan', *Geophysics*, 78(2), pp. B89–B101.

Ramsay, J. G. (1980) 'Shear zone geometry: A review', *Journal of Structural Geology*, 2(1–2), pp. 83–99.

Reid, J. E. *et al.* (2006) 'Unambiguous apparent conductivity for fixed-loop transient electromagnetic data', *Exploration Geophysics*, 37(4), pp. 348–354.

Ritter, O. *et al.* (2003) 'Geophysical images of the Dead Sea Transform in Jordan reveal an impermeable barrier for fluid flow', *Geophysical Research Letters*, 30(14), pp. 2–5.

Ritter, O. *et al.* (2005) 'Electrical conductivity images of active and fossil fault zones', *Geological Society, London, Special Publications*, 245(1), pp. 165–186.

Selway, K. (2014) 'On the Causes of Electrical Conductivity Anomalies in Tectonically Stable Lithosphere', *Surveys in Geophysics*, 35(1), pp. 219–257.

Selway, K., Thiel, S. and Key, K. (2012) 'A simple 2-D explanation for negative phases in TE magnetotelluric data', *Geophysical Journal International*, 188(3), pp. 945–958.

Shankland, T. J. and Ander, M. E. (1983) 'Electrical conductivity, temperatures, and fluids in the lower crust', *Journal of Geophysical Research: Solid Earth*, 88(B11), pp. 9475–9484.

Simpson, F. and Bahr, K. (2005) *Practical Magnetotellurics*, *Cambridge University Press*.

Soille, P. and Vincent, L. M. (1990) 'Determining watersheds in digital pictures via flooding simulations', *Proc. SPIE*, pp. 240–250.

Sternberg, B. K., Washburne, J. C. and Pellerin, L. (1988) 'Correction for the static shift in magnetotelluics using transient electromagnetic soundings', *Geophysics*, 53(11).

Stesky, R. M. (1986) 'Electrical conductivity of brine-saturated fractured rock', *Geophysics*, 51(8), pp. 1585–1593.

Sun, J. *et al.* (2003) 'Sounding of electrical structure of the crust and upper mantle along the eastern border of Qinghai-Tibet Plateau and its tectonic significance', *Science in China Series D-Earth Sciences*, 46(October), p. 243–+.

Szarka, L. (1987) 'Geophysical aspects of man-made electromagnetic noise in the earth-A review', *Surveys in Geophysics*, 9(3–4), pp. 287–318.

Unsworth, M. and Bedrosian, P. A. (2004) 'On the geoelectric structure of major strike-slip faults and shear zones', *Earth, Planets and Space*, 56(12), pp. 1177–1184.

Unsworth, M., Egbert, G. and Booker, J. (1999) 'High-resolution electromagnetic imaging of the San Andreas fault in Central California', *Journal of Geophysical Research*, 104(10), pp. 1131–1150.

Unsworth, M. J. *et al.* (1997) 'Internal structure of the San Andreas fault at Parkfield, California', *Geology*, 25(4), pp. 359–362.

Vernon, R. H. *et al.* (1995) 'Large volumes of anhydrous pseudotachylyte in the Woodroffe Thrust, eastern Musgrave Ranges, Australia', *Journal of Structural Geology*, 17(3), pp. 371–383.

Waff, H. S. and Weill, D. F. (1975) 'Electrical Conductivity of Magmatic Liquids: Effects of Temperatures, Oxygen Fugacity and Compostion', *Earth and Planetary Science Letters*, 28, pp. 254–260.

Wang, D. *et al.* (2006) 'The effect of water on the electrical conductivity of olivine', *Nature*, 443(7114), pp. 977–980.

Wang, H. *et al.* (2017) 'Measurement and visualization of tight rock exposed to CO2 Using NMR Relaxometry and MRI', *Scientific Reports*, 7(44354), pp. 1–10.

Watson, H. C., Roberts, J. J. and Tyburczy, J. A. (2010) 'Effect of conductive impurities on electrical conductivity in polycrystalline olivine', *Geophysical Research Letters*, 37(1), pp. 1–6.

Wex, S. *et al.* (2015) 'Geometry of a large-scale low-angle mid-crustal thrust (Woodroffe Thrust, Central Australia)', *EGU General Assembly*, 17(1).

Xu, Y. *et al.* (1998) 'Electrical Conductivity of Olivine, Wadsleyite, and Ringwoodite Under Upper-Mantle Conditions', *Science*, 280(5368), pp. 1415–1418.

Xu, Y., Shankland, T. J. and Poe, B. T. (2000) 'Laboratory-based electrical conductivity in the

Earth's mantle', *Journal of Geophysical Research*, 105(B12), pp. 27865–27875.

Yang, X. *et al.* (2011) 'Effect of water on the electrical conductivity of lower crustal clinopyroxene', *Journal of Geophysical Research: Solid Earth*, 116(4).

Yang, X. (2011) 'Origin of High Electrical Conductivity in the Lower Continental Crust: A Review', *Surveys in Geophysics*, 32(6), pp. 875–903.

Yang, X. (2012) 'An experimental study of H solubility in feldspars: Effect of composition, oxygen fugacity, temperature and pressure and implications for crustal processes', *Geochimica et Cosmochimica Acta*. Elsevier Ltd, 97(1), pp. 46–57.

Yang, X. *et al.* (2012) 'Electrical conductivity of orthopyroxene and plagioclase in the lower crust', *Contributions to Mineralogy and Petrology*, 163(1), pp. 33–48.

Yang, X. and Heidelbach, F. (2012) 'Grain size effect on the electrical conductivity of clinopyroxene', *Contributions to Mineralogy and Petrology*, 163(6), pp. 939–947.

Yoshino, T. *et al.* (2006) 'Hydrous olivine unable to account for conductivity anomaly at the top of the asthenosphere', *Nature*, 443(7114), pp. 973–976.

Yoshino, T. *et al.* (2012) 'Effect of temperature, pressure and iron content on the electrical conductivity of olivine and its high-pressure polymorphs', *Journal of Geophysical Research: Solid Earth*, 117(8), pp. 1–16.

Yoshino, T. and Noritake, F. (2011) 'Unstable graphite films on grain boundaries in crustal rocks', *Earth and Planetary Science Letters*. Elsevier B.V., 306(3–4), pp. 186–192.

Zhao, G. *et al.* (2012) 'Crustal structure and rheology of the Longmenshan and Wenchuan Mw 7.9 earthquake epicentral area from magnetotelluric data', *Geology*, 40(12), pp. 1139–1142.

8 Supplementary Figures

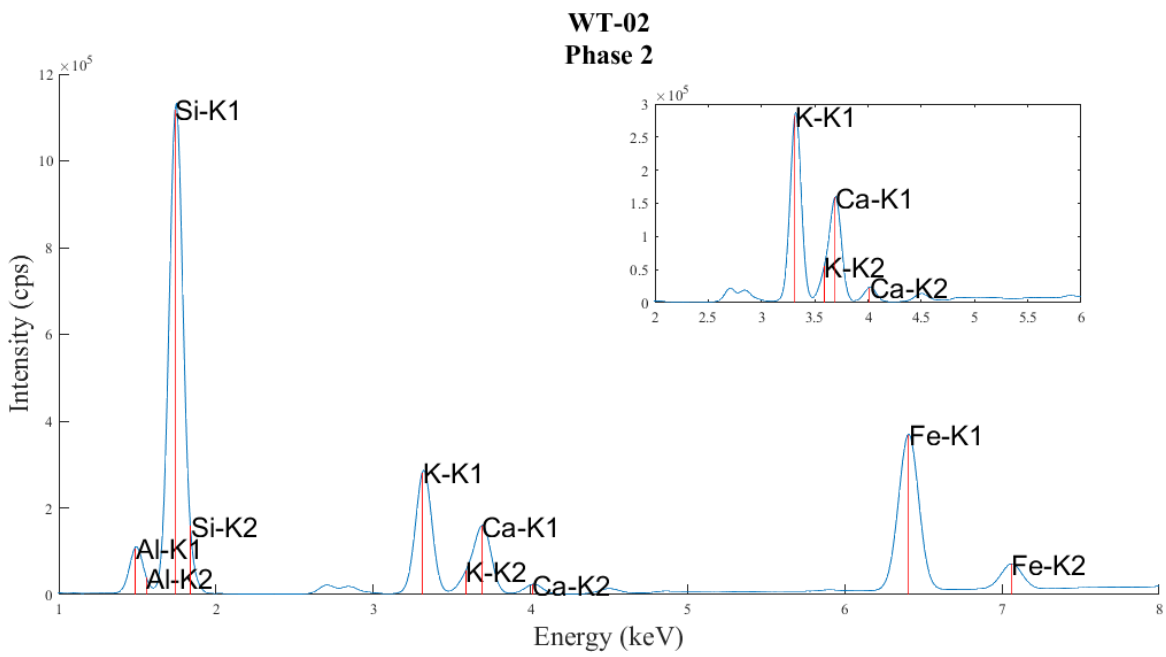

Supp.Figure 1 - Characteristic spectrum identified as quartz due to the high Si count, Note the other elemental peaks are genuine values but they are associated with errors introduced by our point size. Note the Fe count as this is a common theme throughout all characteristic spectrums.

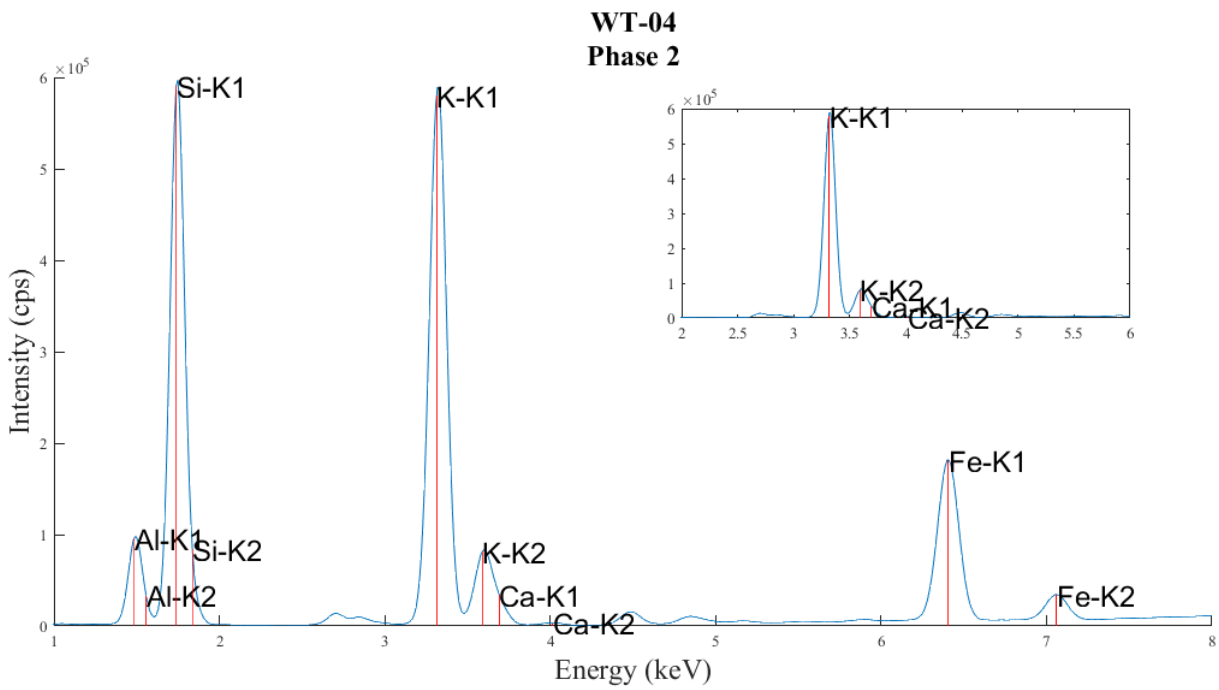

Supp.Figure 2- Characteristic spectrum which as K-Feldspar due to the high K and Si count. Note again the Fe count as this is a common theme throughout.

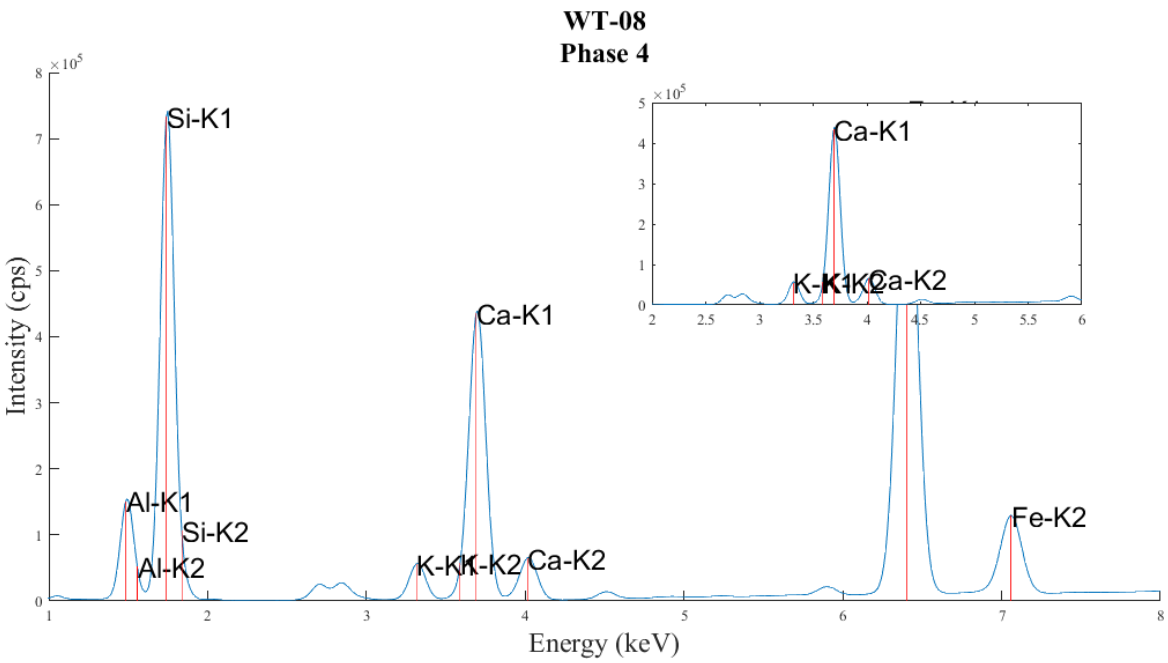

Supp.Figure 3 - Characteristic spectrum identified as Anorthite due to the high Ca count.

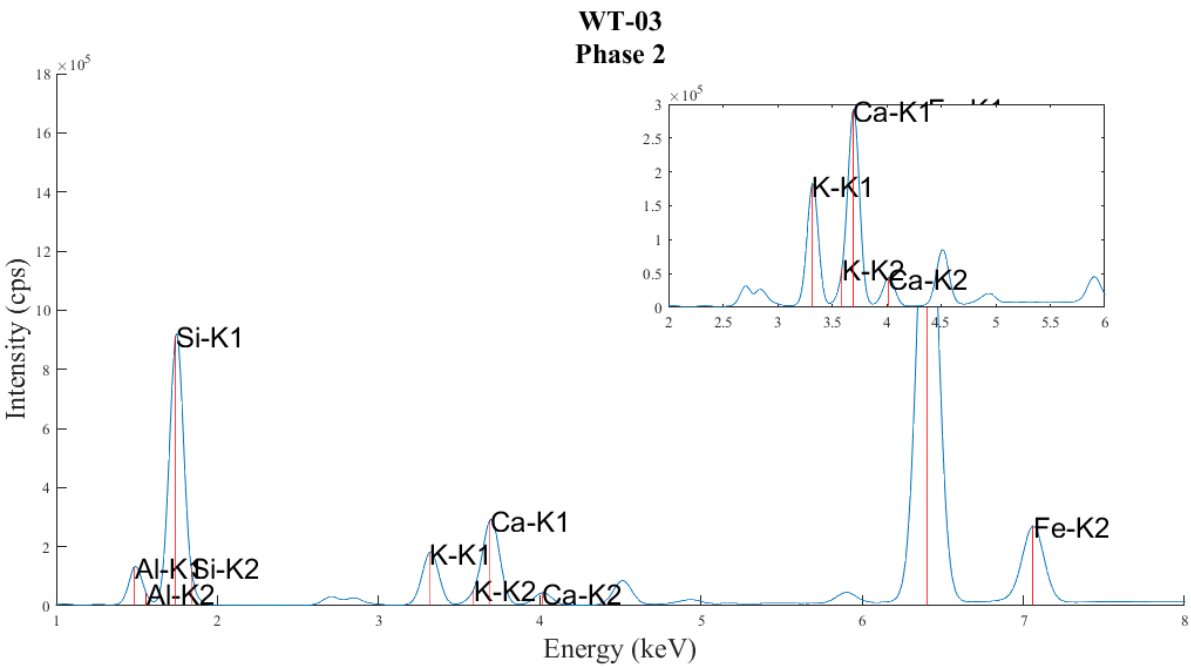

Supp.Figure 4 - Characteristic spectrum which was identified as groundmass due to the distinct elemental peaks which do not directly correspond with a specific single mineral. It is likely that this phase corresponds to a collection of the responses of multiple aphanitic grains which are being averaged by the relatively large spot size. Note again the Fe count.

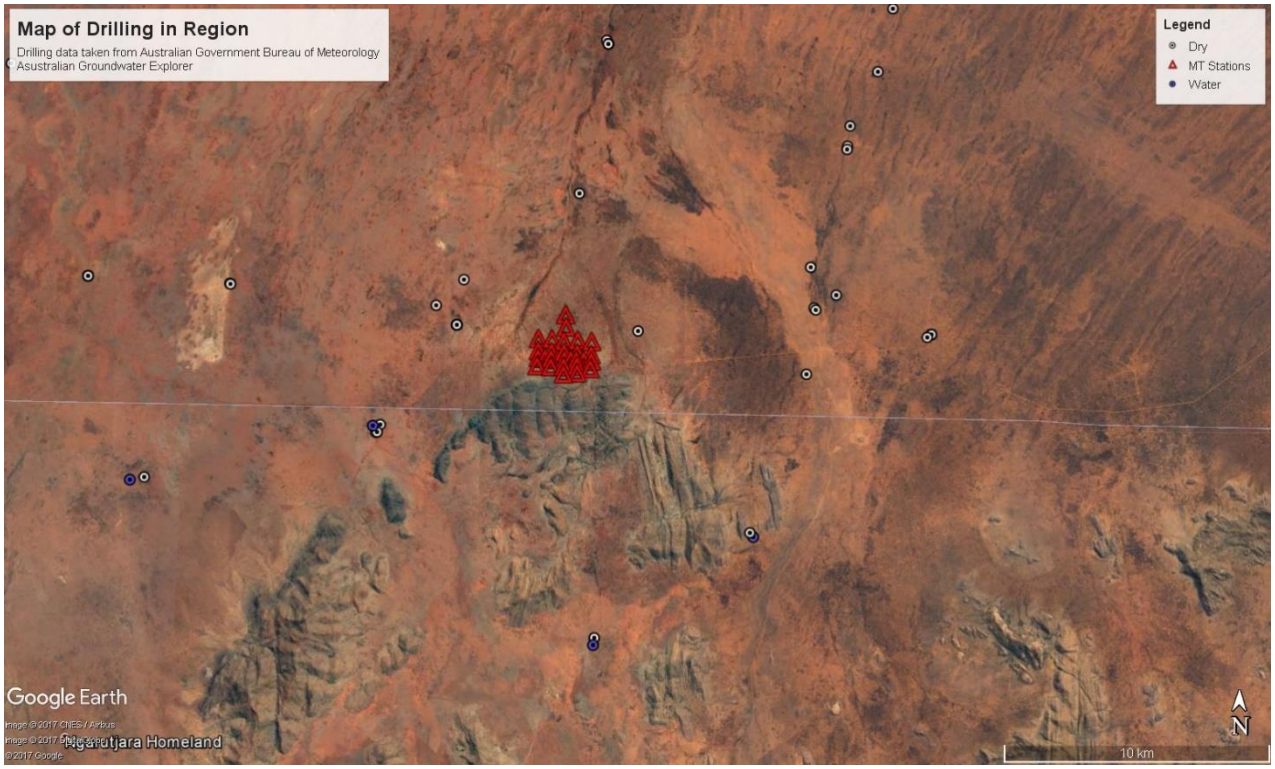

Supp.Figure 5 - Map showing bore data (Australian Government : Bureau of Meteorology, 2017) *and associated water finds relative to MT stations of* Selway et. al., (2012*).*